



Optimizing the structure and movement of a robotic bat with biological kinematic synergies

The International Journal of
Robotics Research
2018, Vol. 37(10) 1233–1252
© The Author(s) 2018
Article reuse guidelines:
sagepub.com/journals-permissions
DOI: 10.1177/0278364918804654
journals.sagepub.com/home/ijr
SAGE

Jonathan Hoff^{1,2}, Alireza Ramezani³, Soon-Jo Chung³ and Seth Hutchinson^{1,2,4}

Abstract

In this article, we present methods to optimize the design and flight characteristics of a biologically inspired bat-like robot. In previous, work we have designed the topological structure for the wing kinematics of this robot; here we present methods to optimize the geometry of this structure, and to compute actuator trajectories such that its wingbeat pattern closely matches biological counterparts. Our approach is motivated by recent studies on biological bat flight that have shown that the salient aspects of wing motion can be accurately represented in a low-dimensional space. Although bats have over 40 degrees of freedom (DoFs), our robot possesses several biologically meaningful morphing specializations. We use principal component analysis (PCA) to characterize the two most dominant modes of biological bat flight kinematics, and we optimize our robot's parametric kinematics to mimic these. The method yields a robot that is reduced from five degrees of actuation (DoAs) to just three, and that actively folds its wings within a wingbeat period. As a result of mimicking synergies, the robot produces an average net lift improvement of 89% over the same robot when its wings cannot fold.

Keywords

Aerial robotics, biologically inspired robots, kinematics

1. Introduction

Animals are living and working solutions to the complex problems of kinematics, dynamics, and control; understanding these biological systems can give incredible insight into designing new robotic systems. These biological organisms can provide the framework for building a robot and implementing its desired motion as well as give intuition for control strategies. However, it is often difficult to incorporate the many complexities of a biological system when building a robot. The design of these robots is thus often focused on finding redundancies in the structure and designing a robotic system with a lower complexity than the original system. For example, the human hand is a system with over 20 degrees of freedom (DoFs) (Lin et al., 2000). Robotic grippers and hands are often built to embody the unique grasping capabilities of the human hand while having a reduced number of DoFs to minimize the required number of actuators and to reduce computation. Thus, production is more feasible, and implementation of robotic grippers and hands becomes more practical. For example, the Pisa/IIT SoftHand has 19 DoFs but uses only a single actuator for control (Catalano et al., 2014, 2012). Another example is the DLR-Hand II, which is a robotic gripper that was

designed to have 13 DoFs, giving it a lower-dimensional configuration space than the human hand (Butterfaß et al., 2001).

Similarly, flying robots have been designed to mimic insects (Deng et al., 2006a,b; Ma et al., 2013), birds (Paranjape et al., 2013; Shyy et al., 2010), hummingbirds (Keennon et al., 2012), and bats (Bahlman et al., 2013; Chung and Dorothy, 2010; Colorado et al., 2012; Ramezani et al., 2017, 2015, 2016a,b). The flight mechanisms found in these biological creatures are often very complex, and

¹Department of Electrical and Computer Engineering, University of Illinois at Urbana-Champaign, Urbana, IL, USA

²Coordinated Science Laboratory, University of Illinois at Urbana-Champaign, Urbana, IL, USA

³Graduate Aerospace Laboratories, California Institute of Technology, Pasadena, CA, USA

⁴School of Interactive Computing, Georgia Institute of Technology, Atlanta, GA, USA

Corresponding author:

Jonathan Hoff, Department of Electrical and Computer Engineering and Coordinated Science Laboratory, University of Illinois at Urbana-Champaign, Urbana, IL, 61801, USA.

Email: jehoff2@illinois.edu

mimicking them precisely is a substantial undertaking. Thus, researchers have analyzed these biological creatures in attempts to create an artificial system that can roughly mimic their behaviors while having a simplified design.

In designing bio-inspired robots, a simplified architecture is derived from observing biology and then searching for redundancies and reducing complexity. The resulting robot is often considered suitable and the structure is left as is. However, it can be advantageous to add a second stage to the design process. Specifically, the structure and movement of the robot can be modified such that its kinematic behavior more closely mimics biology, and this can result in performance improvements. In this article, we claim that more closely mimicking biology's dominant kinematic synergies and their timed activations can in fact improve robot performance. Specifically, we consider the process of designing a robotic bat from observations of biology.

Bats have a very sophisticated flight mechanism, possessing over 40 DoFs (Riskin et al., 2008). These animals have been studied for many years, but only recently have researchers attempted to mimic them (Bahlman et al., 2013; Chung and Dorothy, 2010; Colorado et al., 2012). Several studies were conducted to design and construct a robotic bat based on observations of biological bats in nature (Ramezani et al., 2017, 2015, 2016a,b). The development of a bat-size aerial robot is constrained by weight, size, and power limitations (Pines and Bohorquez, 2006; Platzer et al., 2008). Furthermore, mimicking the kinematics of a biological bat is challenging because of its complex morphology. Implementing a bat's 40 DoFs as a robot would require a very large number of actuators. Given the strict weight requirements necessary for flapping flight and the current limitations of technology, it is essentially infeasible to do this. Simplifications are therefore required for flight to be possible. These restrictions and limitations have motivated better understanding and selection of major DoFs in biological bats.

The robotic Bat-Bot (B2) was designed to possess the morphing properties of bat wings and retain their dominant motions found in flight while having only five degrees of actuation (DoAs) (Ramezani et al., 2017, 2015, 2016a,b). The DoAs are synchronous flapping, asynchronous folding and unfolding movements of the wings, and stabilizing movements of the hindlimbs. This low-dimensional design was formulated by first analyzing the skeletal structure of biological bats and their dominant movements. In addition, groups of joints in bats have been shown to move together during flight through analysis of recorded motion capture data of bats flying in a wind tunnel (Riskin et al., 2008). B2 was designed to exploit these groups. The resulting construction has a reduced dimensional complexity but retains motion abilities similar to the studied organism.

In an effort to more closely mimic biology, this article presents a second stage design methodology that assumes the existing topology of B2. This synergistic approach uses optimization to modify structural parameters affecting wing geometry and select ideal actuator trajectories such that the

kinematic synergies and activations of the robot most closely match those of a biological bat. This optimization routine compares the synergies obtained from prerecorded trajectories of markers on a biological bat to equivalent simulated marker trajectories on B2. The performance functional consists of the sum of squared differences between Euclidean positions of the markers of the biological bat and B2 reconstructed after performing principal component analysis (PCA) with only the first two components. The improved matching of B2's kinematics to biology is validated both in simulation and motion capture experiments. Furthermore, load cell experiments of the new system confirm improvements in lift production. Negative lift during the upstroke is reduced because B2 folds its wings during the upstroke, and on average there is an 89% improvement in net lift generation over a wingbeat period.

This is consistent with the literature of biological bat flight: it is thought that bats fold their wings during the upstroke portion of the wingbeat period to improve efficiency and reduce negative lift (Riskin et al., 2012), and this has been experimentally verified with a robotic bat wing (Bahlman et al., 2013). As seen from Hoff et al. (2016), folding and unfolding the wings of B2 within a wingbeat period is the necessary synergy activation that must occur to mimic biology. However, the on-board motors driving wing folding of the previous design of B2 (Ramezani et al., 2017) are unable to synchronize folding with flapping, and thus wing folding cannot occur within the required time window. Therefore, we redesigned the actuation system based on the works in (Hoff et al., 2017) to couple folding and flapping such that the principal component activations can be realized.

The work in this article is organized as follows. Section 2 provides background information regarding synergies and bio-inspired robots built to mimic synergies. Section 3 describes the biological bat motion capture data, which will be compared against the behavior of B2. The construction and capabilities of B2 are detailed in Section 4. Specifically, it provides information regarding the structural design of B2 and derives a parametric kinematic model that expresses the markers' positions in terms of the optimization variables, i.e., the position of the actuated coordinates and the physical parameters of B2. Using this model, Section 5 presents the optimization formulation that finds the actuator trajectories over the wingbeat cycle of B2 and its structural parameters by comparing prerecorded trajectories of markers on a biological bat to B2's equivalent marker trajectories. The optimization results from simulation and the experimental results are presented in Section 6. Concluding remarks are made in Section 7. It should be noted that the works in parts of this study have previously been published in the conference proceedings of Hoff et al. (2016) and Hoff et al. (2017).

2. Synergies

Kinematic synergies of biological bats are the foundation for the work in this study as they are used to optimize B2's

behavior to that of a biological bat. In this section, we review the concept of kinematic synergies. We provide a brief literature review of the use of synergies in studying biological organisms, and we give examples of robot designs inspired by synergies in biology.

2.1. Background

The movement of humans and animals has been a much studied topic. The concept of muscle synergies has proved particularly useful in these studies. This theory of unified activations within groupings of muscles was first proposed by Bernstein (1967), and it is based on the assumption that it is very difficult for the central nervous system to independently control all of the joints of an animal independently. In humans, for example, many movements are a cooperative effort from different muscle groups. A study on postural control in humans analyzed electromyography (EMG) activity of 16 muscles in the back and legs of humans (Torres-Oviedo and Ting, 2007), and it reported that six or fewer muscle synergies were able to accurately replicate the postural responses. Similarly findings have been discovered in animals: researchers have explained the kicking motion in frogs with three time-varying muscle synergies (d'Avella et al., 2003).

The kinematic movements produced from these muscle synergies likewise have synergies of their own. Numerous studies have been performed to quantify the set of synergies of humans and animals to characterize their behavior in a low-dimensional space. These synergies often form a set of basis vectors of which only the most dominant are needed to approximate the animal's movement. For example, one DoF in animals may correspond to the coordinated movement of multiple joints (Bernstein, 1967). One DoF is not necessarily expressed only as one joint because often movements of joints are coupled to each other. Studies have frequently used the statistical method PCA to reduce the dimensions of a data set (Jolliffe, 2002).

PCA has been successful in identifying the synergies of human movement. Daffertshofer et al. (2004) demonstrated that human walking could be accurately explained with only a few principal components from kinematic and EMG data. PCA has also been effective in human gait recognition (Wang et al., 2003), studying walking and running gaits (Cappellini et al., 2006), and identifying kinematic synergies of human arm movement (Fod et al., 2002). As a result, these methods have been applied to the design of humanoid robots and robotic arms. Taix et al. (2013) optimized the movement of a humanoid robot performing reaching motions to match those of a human, and it encoded these movements as motor primitives in the robot using PCA. Natural human-like arm motion can be generated by a robotic arm using linear combinations of principal components, i.e., kinematic synergies of the human arm (Lim et al., 2005). PCA has also been used to reduce the dimensional complexity of the EMG signals and the joint angles

of the human arm to control an anthropomorphic robotic arm (Artemiadis and Kyriakopoulos, 2010).

Robotic hand research has been powered by representing grasping in a low-dimensional space. The human hand has become a widely studied kinematic structure for synergies, and this has been useful in the design of robotic hands. Santello et al. (1998) showed that greater than 80% of the variance of static grasping data can be described by only the first two postural synergies, i.e., principal components. From these results, Brown and Asada (2007) designed a robotic hand with the kinematic topology of a human hand that could be actuated with only two motors controlling the first two postural synergies. Similarly, Ciocarlie et al. (2007); Ciocarlie and Allen (2009) expanded upon the analyses of Santello et al. (1998) through grasp planning using these first two postural synergies. This research in synergies has been further developed by the idea of "soft synergies" presented by Bicchi et al. (2011) and Gabbicini et al. (2011), and these have been implemented on the anthropomorphic Pisa/IIT SoftHand (Catalano et al., 2014).

The efforts in quantifying complex behavior of biological mechanisms in a lower-dimensional subspace have led to the successful design of bio-inspired robots that can mimic their biological counterparts to a great extent in spite of retaining fewer DoFs. Kinematic analysis of biological data of frogs jumping guided the creation of the mechanical design of frog legs with fewer DoFs (Wang et al., 2008). Snakes have kinematic synergies, and these have been extracted and implemented on a snake robot (Gong et al., 2016). Crickets have been analyzed with high-speed video to identify important parts of the kinematic structure of their legs (Laksanacharoen et al., 2000), and this has led to the successful design of a cricket robot (Birch et al., 2000). Images of sequential side view shots of kangaroos were used to create a kangaroo robot with fewer DoFs (Liu et al., 2014). Development of the MIT Robotic Cheetah was aided with the analysis of tendon–bone locations of biological legged systems (Ananthanarayanan et al., 2012). Tangorra et al. (2007) developed a robotic fish by first analyzing the kinematics of the pectoral fin of a sunfish to design the robot in a low-dimensional space. It used PCA in its analysis of the sunfish to extract the three most dominant modes that made up 67% of the variance and implemented these on the robotic fin.

Flapping flight has also borrowed from low-dimensional analysis. Like the human hand, it is imperative to recognize the sophisticated complexity of a biological bat's flight apparatus. It possesses ball-and-socket and revolute joints that connect the bones and muscles to one another and synthesize a metamorphic musculoskeletal system with over 40 DoFs. It is known that some of these joints are passive whereas some are active (Riskin et al., 2008). Similar to the previously mentioned research, bat motion can be described in a low-dimensional space using PCA. There are three groupings of joints in a bat wing that move together, accounting for 14 of 20 joints (Riskin et al., 2008). This experiment also discovered that approximating the bat's

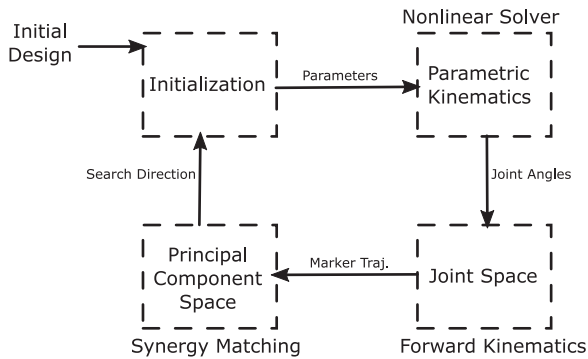


Fig. 1. Proposed PCA-based synergistic design framework to effectively draw a connection between prohibitively hard-to-copy biological organisms with non-trivial morphologies and bio-inspired robot designs.

motion with only 16 of 46 principal components accounted for 95% of the variance of the original behavior, and the first two principal components represent 57% of the variance. These observations of bat flight suggest that the dimensional complexity can be significantly reduced by making correlations between couplings of the bat's kinematics. By choosing only some of the principal components, the dimensionality of the bat can be reduced without much loss of the accuracy of reproducing the actual data. As mentioned earlier, B2's initial design was motivated by these observations of synergies in bats, and it was given folding–unfolding and flapping capabilities to match these dominant synergies.

2.2. Synergistic design approach

As seen in the previous examples, synergies offer a means for describing biology at a more fundamental level, and they are effective for the initial stage of designing the kinematic structures of bio-inspired robots. This stage is shaped by the selection of a general structural topology that will define the capabilities of the robot. We propose that a second stage of design can be built upon this first stage. This design framework illustrated in Figure 1. It assumes this selected topology and actuator placement as the initial design, and it attempts to adapt the design from the first stage to match biology more closely. This requires quantifying the behavior of biology and the robot and comparing them in the same mathematical space. However, this is challenging because biology is often very complex, and exactly mimicking it is not possible. Consequently, the most important features buried in the complexities of biology must be extracted to aid in this comparison. PCA offers an excellent solution to quantifying behavior and obtaining the dominant characteristics in the form of kinematic synergies. This method has been successful in numerous areas of biology and has been shown to accurately describe complex systems in a low-dimensional space. It eliminates the complexities in biology and extracts only the most important qualities relevant to the robot. Given these biological synergies from PCA, the robot's synergies must likewise be

extracted for comparison. This requires several steps to map design parameters to synergies in the principal component space. First, a parametric kinematic model maps the design parameters and motor inputs to the joint space. These joint angles are then input into the forward kinematics to produce the 3D motion of the system. Finally, synergies are derived from the output of the forward kinematics, thus allowing the evaluation of the current selection of parameters and motor inputs. This iterative routine delivers a new set of design parameters such that the system more closely copies the dominant synergies of biology.

In bats, flapping and folding are the two most dominant synergies. Given the design of B2, using optimization to match only the two most dominant synergies results in the wings flapping and the wings folding at a particular time in the period. PCA takes out the complexities that B2 cannot match. The results of PCA of biological bat data reported by Riskin et al. (2008) offer a means for describing bat kinematics in a low-dimensional space. Furthermore, analysis of the skeletal structures of a biological bat wing and a human hand shows great similarities between the two structures. Although grasping is not periodic, i.e., it is not a gait cycle like flapping in bats, the structural similarities between hands and bat wings and the success of implementing PCA for designing robotic hands are encouraging to the validity of our synergistic optimization approach to be applied to the flight mechanism of B2.

3. Motion capture data

Some bio-inspired robots have been rigorously designed by analysis of kinematic data of their biological counterparts. Experiments in this area are typically conducted to analyze the behavior of biological systems on a more quantitative level. One technique used in the literature to interpret kinematics involves setup of high-speed cameras to track the motion of the animal (Hubel et al., 2012; Riskin et al., 2008; Tian et al., 2006). Reflective markers are attached to the animal, and its motion is recorded. Post-processing methods are used to find Cartesian coordinates of the markers over a time period. This spatiotemporal motion capture data contains the kinematic behavior of the animal in terms of the evolution of the attached markers in the Cartesian coordinate frame over time. This data provides further quantitative information that can aid in the design of robots. Studies of flapping flight have used this experimental procedure (Hubel et al., 2012; Riskin et al., 2008). Other studies have used similar experimental setups to quantify the kinematic behavior of grasping of the hand (Mason et al., 2001; Santello et al., 1998).

The design of a robot with bat morphology that emulates the synergistic behavior of a biological bat can be improved with analysis of data describing its kinematics over a wing-beat cycle. We used high-speed motion capture data of *Tadarida brasiliensis* provided by researchers Dr. Kenneth Breuer and Dr. Sharon Schwartz from Brown University

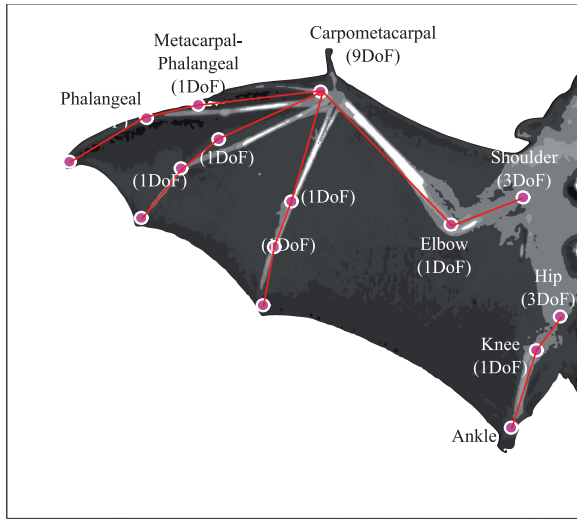


Fig. 2. DoFs of a biological bat. In producing this figure, an image from Riskin et al. (2008) was used.

(Hubel et al., 2012). A detailed description of data collection experiments and post-processing methods that have been used by Brown can be found in Riskin et al. (2008), though a different bat species was used for the results in that study. Three Photron 1024 PCI digital high-speed cameras (Photron USA, Inc., San Diego, CA USA) recorded whole wing and body kinematics of bats in a wind tunnel at 1000 Hz with 1024×1024 pixel resolution. The marker positions were digitized to 3D positions by using the direct linear transformation (DLT) method on the recorded 2D images. Post-processing filled in gaps using polynomial fitting.

The marker locations are shown in Figure 2. This selection of markers was determined by careful analysis of the dimensional complexity for varying marker placement (Riskin et al., 2008). The kinematic data set consists of the Cartesian coordinates of these data points that were tracked by high-speed cameras. We denote by n the number of time samples for a single wingbeat cycle of a bat, with each sample containing the Cartesian coordinates for $n_p = 17$ data markers placed on the bat. The position vectors of the markers are in the form $\mathbf{p}_i = [x_i \ y_i \ z_i]^T$, and these are used to build a *data matrix* of the form

$$\mathcal{M} = \begin{bmatrix} \mathbf{p}_1(t_1)^T & \mathbf{p}_2(t_1)^T & \cdots & \mathbf{p}_{n_p}(t_1)^T \\ \mathbf{p}_1(t_2)^T & \mathbf{p}_2(t_2)^T & \cdots & \mathbf{p}_{n_p}(t_2)^T \\ \vdots & \vdots & \vdots & \vdots \\ \mathbf{p}_1(t_n)^T & \mathbf{p}_2(t_n)^T & \cdots & \mathbf{p}_{n_p}(t_n)^T \end{bmatrix}. \quad (1)$$

The term $\mathbf{p}_i(t_j)$ refers to Cartesian coordinate vector of marker i at time sample j .

3.1. Data preprocessing

The original data set has a Cartesian coordinate system based on an inertial frame of reference fixed at a point in the wind tunnel. We introduced a body-referenced coordinate frame about the anterior marker of the biological bat.

The origin is the anterior sternum marker. The x axis passes from the posterior sternum marker to the anterior sternum marker. The y axis is orthogonal to the x axis and gravity. The z is orthogonal to the other two axes. This is the coordinate system used by Riskin et al. (2008).

It should be noted that Ramezani et al. (2016a) designed B2 based on the dimensions of *Rousettus aegyptiacus*. This bat is much larger bat than *Tadarida brasiliensis* (the bat used for the analyses in this article). Owing to this discrepancy, we scaled the data for *Tadarida brasiliensis* such that the outstretched wingspan $B_{T.b.}$ for *Tadarida brasiliensis* matches the outstretched wingspan $B_{R.a.}$ of *Rousettus aegyptiacus* (Norberg, 1972; Norberg and Rayner, 1987). The subscript T.b. refers to *Tadarida brasiliensis*, and the subscript R.a. refers to *Rousettus aegyptiacus*.

4. Construction and parameterization

In our previous work, analysis of biological bats led to the design of a flapping robot with bat morphology (Ramezani et al., 2015, 2016a,b). These studies designed the structure and capabilities of the robot with the intent to mimic the fundamental kinematic synergies observed in biological bats. The two most dominant synergies in a biological bat from PCA are the flapping motion of the wing and the folding and unfolding motion of the wing. B2 was engineered to embody these morphing capabilities as well as dorsoventral hindlimb motion such that it mimics the basic movements of biological bats.

This article contributes to the structural design and the actuator movements of the prototype developed in Ramezani et al. (2016a) by formulating a rigorous optimization routine that matches the principal synergies of B2 to those found in a biological bat and presenting a new mechanism design that can realize these synergies. PCA is used to analyze both the movement of the biological bat and B2 to quantify a representation of the synergies in each. The synergies of the biological bat are embedded in B2 through optimization of its structure and actuator trajectories using the biological bat data described in Section 3. Thus, in this section we provide a description of the construction of an initial prototype of B2 to achieve a basic understanding of its structure. The parametric model of the mechanical constraints and forward kinematics provides mathematical expressions for the marker positions on B2 that will be compared with the marker positions of the biological bat in the optimization routine presented in Section 5. The construction and capabilities of the initial prototype of B2 have been documented in the previous works (Ramezani et al., 2015, 2016a,b). In addition, the new mechanism that couples wing folding–unfolding to flapping has been described in Hoff et al. (2017).

4.1. Robotic bat overview

B2, shown in Figure 3, is designed based on the biological findings that emphasize the existence of functional groups of joints in bats (Ramezani et al., 2015, 2016a,b). There

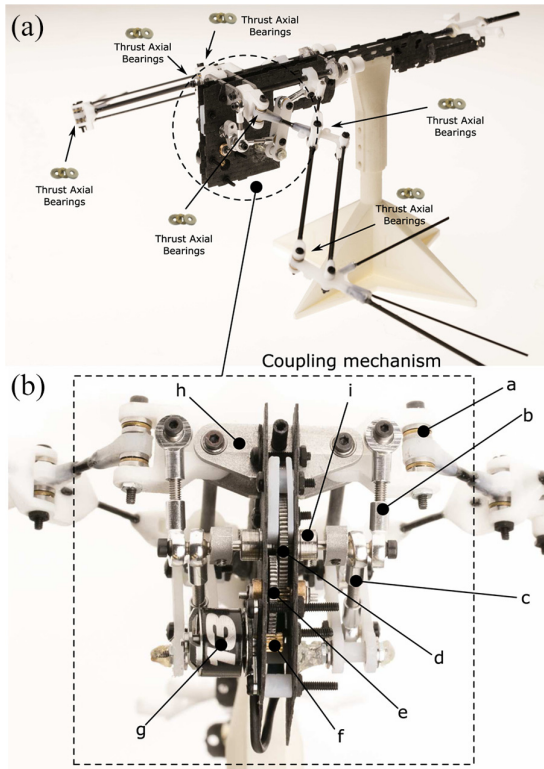


Fig. 3. A: Optimized B2 prototype with coupling mechanism that synchronizes the flapping and wing morphing such that the wings fold in the upstroke and extend in the downstroke. B: Front view of gearbox, coupling mechanism, and crank assembly. (a) Axial thrust bearings for smooth wing morphing, (b) link driving flapping connected to crank, (c) link driving folding–unfolding connected to crank, (d) main spur gear, (e) small spur gear between main gear and pinion gear, (f) pinion gear attached to a brushless DC (BLDC) motor, (g) BLDC motor, (h) aluminum shoulder plate, and (i) stainless steel collar.

are three groups of joints that are coupled in their movements: wrist pronation² and elbow bending; wing spreading and finger bending; and morphing of the medial part of the wings from the combined movement of shoulders, hips, and knees (Riskin et al., 2008). Active actuation of the wrists, fingers, and shoulders is necessary to achieve pronating³ rotation in wrists, humeral rotation, flexion–extension³ motions in digits, and abduction–adduction⁴ motions in digits. However, it is not feasible to design a robotic bat to incorporate all of these DoFs.

A synergistic design approach was employed to incorporate several mechanical linkages in the articulated flight mechanism of B2. The resulting structure has five DoFs. This morphing mechanism requires a minimal number of actuators, while at the same time being capable of producing biologically meaningful movements. These motions include: synchronous flapping motion of the left and right forelimbs, asynchronous mediolateral⁵ motion of each wing (wing folding and unfolding), and asynchronous dorsoventral movement of each leg.

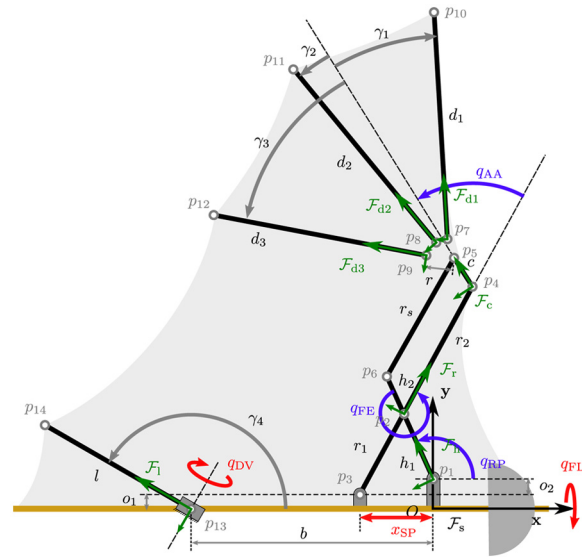


Fig. 4. DoFs and morphological parameters of B2. Gray variables label the marker locations, and black variables describe the structural parameters. The coordinate frames are shown in green. Blue arrows denote biologically meaningful angles in the left forelimb that are not directly actuated. Red arrows show directly actuated angles.

B2’s forelimbs each are constrained to one DoF, shown in Figure 4, providing three coupled active movements: humeral retraction–protraction, elbow flexion–extension, and carpal abduction–adduction. These movements are seen in the shoulder, elbow, and wrist of biological bats and thus are considered biologically meaningful movements. Also similar to a biological bat, B2’s forelimbs provide structural support and the ability to shape the thin synthetic membrane. There are nine links composing each forelimb of B2: the carpal link (p_4 – p_5), the three digital links, the two radial links (p_3 – p_4), the radial support link (p_5 – p_6), and the two humeral links (p_1 – p_6) (Ramezani et al., 2016a). The humeral links are of length h_1 and h_2 . The two radial links have length r_1 and r_2 , and their support has a length of r_s . The forelimb mechanism is manipulated by movement of the spindle, where p_3 is constrained to move along the x axis of the body frame. The humeral link is fixed to the shoulder, and the spindle moves the position of the radial link. The carpal plate and humeral links attach to the radial support link with revolute joints. Elbow flexion–extension is generated from the linear motion of the spindle, as the radial link’s motion is dependent on that of the spindle. Likewise, the digital links attached to the carpal plate move relative to the radial link.

The three fingers are secured to the carpal link of length c . These thin flexible carbon fiber tubes of lengths d_1 , d_2 , and d_3 can passively flex and extend with respect to the carpal plate as well as abduct and adduct with respect to each other. The origin of each is at distance r from the end of the carpal plate p_5 . Unlike biological bats, the digits of B2 lack joints and active actuation. The angles of these digits with respect to the carpal plate are fixed, measuring to be

γ_1 , γ_2 , and γ_3 . Furthermore, B2's carpal links have passive rotations.

The significant movements of the ankles of a biological bat are dorsoventral and mediolateral. In a wingbeat cycle, the upstroke portion consists of dorsal motion and the downstroke consists of ventral motion of the ankle (Cheney et al., 2014). The movement of B2's hindlimbs is limited to dorsoventral movement because mediolateral movement is less dominant in biological bats (Riskin et al., 2008). In addition, B2's hindlimbs (p_{13} – p_{14}) of length l are carbon fiber rods that lack the knee joints present in its biological counterpart. These rods are connected to 1-DoF revolute joints on the tail of its structure, allowing each hindlimb to move in a plane rotated at an angle γ_4 from the parasagittal plane.⁶ The body length between the shoulder and hip is b .

All of these length and angle measurement parameters are lumped into a single-parameter vector

$$\mathcal{P} = [h_1 \quad h_2 \quad r_1 \quad \cdots \quad \gamma_3 \quad \gamma_4]^T \quad (2)$$

This vector gives the exact geometric layout for the given topological structure of B2.

4.2. Coupling mechanism

For our synergistic design scheme effectiveness to be verifiable empirically, we considered a major robot redesign based on coupling the flapping and folding–unfolding movements of B2 (Hoff et al., 2017). In past work we found that to mimic biology, B2's wings must fold and unfold within one wingbeat period, but it was impossible to achieve this high-frequency response with the current motors driving wing folding (Hoff et al., 2016). Therefore, we designed a mechanism (shown in Figure 3) to couple folding–unfolding to flapping such that the wings extend in the downstroke and fold in the upstroke (Hoff et al., 2017). This coupled movement is shown in the video of Extension 1. This synchronization allows B2 to mimic the timed activations of these two dominant synergies found in biology. In this article, we assume this new design and formulate the kinematics based on this paradigm. B2 will have a resulting three DoAs because wing folding is coupled to flapping, and the two DC motors actuating wing morphing have been replaced by a system of linkages.

The kinematics of the system of linkages driving flapping and folding are depicted in Figure 5. We used a four-bar linkage to convert the circular motion of the crank arm (j_3 – j_2) to motion of a rocker (j_4 – j_6). The rocker arm in turn drives the slider (i.e., the spindle). We can characterize the completed motion of this 1-DoF system with the crank angle q_C and the set of parameters describing the lengths of the connections between joints and their offsets. The lengths s_y and s_z denote the offset distance of the shoulder joint j_0 from the crank center j_3 in the $-y$ and z directions. Ball-and-socket joints are attached to the end of the crank arm and to the shoulder. They are connected by link l_1 .

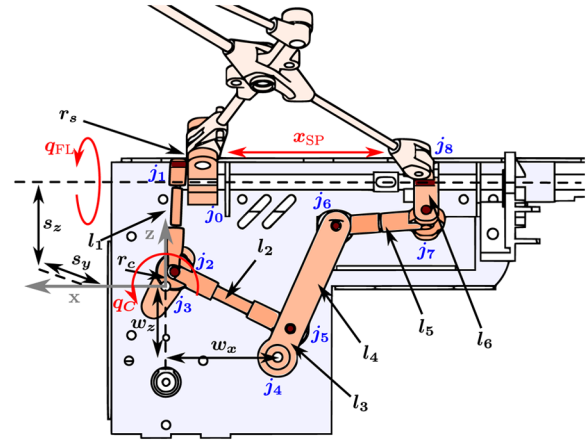


Fig. 5. Side view of the mechanism that couples the flapping and folding motions of B2 (Hoff et al., 2017). Red variables denote changing positions of angles and distance. The structural parameters, i.e., the lengths of links and offsets, are shown in black. Blue variables show joint locations. Joints shaded brown experience both rotation and translation whereas joints in white (j_0 , j_3 , and j_4) have rotation only. The coordinate system (gray) has its y axis pointing out of the page. The linkages are coupled such that there is just one DoF: the crank angle q_C is directly controlled by the BLDC motor, and this in turn characterizes the flapping angle q_{FL} and the spindle position x_{SP} .

The length of the crank radius is r_c , and the shoulder length is r_s , i.e., the distance from j_0 to j_1 .

The four-bar crank-rocker mechanism consists of the drive link r_c , the coupler link l_2 , the rocker l_3 , and the base dimension $\sqrt{w_x^2 + w_z^2}$. Link l_2 converts the rotation of the crank to periodic rocking motion of l_3 about its revolute joint j_4 , which is offset distances of w_x and w_z in the $-x$ and $-z$ directions from j_3 . The rocker arm extends to a length of $l_3 + l_4$ and its end joint j_6 connects to joint j_7 . These ball-and-socket joints are secured to one another by link l_5 . This link in turn drives link l_6 to translate about its prismatic joint j_8 . The rotation of link l_6 about j_8 , however, depends completely on the rotation of the shoulder r_s because the two are joined by the armwing structure. All of the above listed lengths can be combined to give the vector \mathcal{C} .

4.3. Parametric flight kinematics

The static structure of B2 is determined by the physical parameters vector \mathcal{P} , but the evolution of its kinematics during flight requires characterizing the actuators that drive its motion over a wingbeat cycle. For the purposes of this study, only consideration of one wing is necessary as it shall be assumed that the wings mirror each other in straight flight. In addition, the coupling mechanism forces identical behavior of the two wings when the wing parameters \mathcal{P} are the same on each side. The actuated coordinates, which express the positions of the actuators, are denoted by

$$\mathcal{Q}_a = [q_C \quad q_{DV}]^\top \quad (3)$$

where q_{DV} is the dorsoventral angle (the angle the hindlimb makes with respect to the x - y plane, shown in Figure 4).

The configuration variable vector

$$\mathcal{Q} = [q_{RP} \quad q_{FE} \quad q_{AA} \quad x_{SP} \quad q_{FL} \quad q_{DV}]^\top \quad (4)$$

defines the shape of the wing and hindlimb as it evolves through the action of actuated coordinates. The terms q_{RP} , q_{FE} , q_{AA} , q_{FL} , and q_{DV} are the five biologically meaningful angles of B2, as shown in Figure 4. The angle q_{RP} denotes the retraction and protraction angle, q_{FE} the radial flexion and extension angle, q_{AA} the abduction and adduction angle of the carpus, q_{FL} the flapping angle (the angle that wing makes with respect to the x - y plane), and q_{DV} the dorsoventral movement of the hindlimb. The term x_{SP} is the position of the spindle that moves linearly to control the folding-unfolding of the wing. The angles q_{RP} , q_{FE} , and q_{AA} move in response to this term.

4.4. Structural constraints

The relationship between \mathcal{Q}_a and \mathcal{Q} is defined by nonlinear mappings, and these mappings can be derived analytically by imposing the appropriate mathematical constraints on the system.

4.4.1 Crank constraints. First, the nonlinear mapping

$$\mathcal{G}_{\text{crank}} : (q_C, \mathcal{C}) \mapsto (x_{SP}, q_{FL}) \quad (5)$$

describes the dependency of spindle position x_{SP} and the flapping angle q_{FL} on the position of the crank angle q_C and the selection of the values for the crank parameters \mathcal{C} . The mechanical system of linkages is shown in Figure 5. It is a 1-DoF system that depends solely on q_C and the values of \mathcal{C} . We can enforce this by imposing a set of kinematic constraints on this closed-loop kinematic chain.

We determine q_{FL} by considering the closed loop j_0 - j_1 - j_2 - j_3 . We establish the loop closure by ensuring that l_1 has constant length by adding its projections onto the \mathbf{xy} , \mathbf{xz} , and \mathbf{yz} planes as

$$2l_1^2 = l_{1,xy}^2 + l_{1,xz}^2 + l_{1,yz}^2 \quad (6)$$

The projections $l_{1,xy}$, $l_{1,xz}$, and $l_{1,yz}$ are functions of the known variables s_y , s_z , r_C , r_s , and q_C , and the unknown variable q_{FL} . Algebraic manipulations produce the equation of form

$$A \cos q_{FL} + B \sin q_{FL} + C = 0 \quad (7)$$

in which A , B , and C are functions of q_C and \mathcal{C} . This is equivalent to Freudenstein's equation, and thus q_{FL} can be solved for as a quadratic by making trigonometric substitutions for $\sin q_{FL}$ and $\cos q_{FL}$.

Next, we consider the remaining mechanism to derive an expression of x_{SP} . We solve the planar four-bar linkage by deriving the closure equations for loop j_2 - j_3 - j_4 - j_5 . This is equivalent to forcing the vectors traversing the linkage to sum to zero, i.e., the loop is closed. This is written as

$$\vec{j_3j_2} + \vec{j_2j_5} + \vec{j_5j_4} + \vec{j_4j_3} = 0 \quad (8)$$

The sum of the vectors around the linkage must equal zero for the loop to remain closed. We expand these terms as

$$\begin{aligned} & \text{Rot}_y(\phi_3) \begin{bmatrix} r_c \\ 0 \\ 0 \end{bmatrix} + \text{Rot}_y(\phi_2) \begin{bmatrix} l_2 \\ 0 \\ 0 \end{bmatrix} \\ & + \text{Rot}_y(\phi_5) \begin{bmatrix} l_3 \\ 0 \\ 0 \end{bmatrix} + \text{Rot}_y(\phi_4) \begin{bmatrix} \|w\| \\ 0 \\ 0 \end{bmatrix} = 0 \end{aligned} \quad (9)$$

where $\|w\| = \sqrt{w_x^2 + w_z^2}$ and ϕ_2 , ϕ_3 , ϕ_4 , and ϕ_5 are the respective angular positions of joints j_2 , j_3 , j_4 , and j_5 . Rot_y is the rotation matrix about the y axis. The base link is stationary, thus ϕ_4 is a known constant that remains at position $\phi_4 = 2\pi - \text{atan} \frac{w_z}{w_x}$. Angle ϕ_3 is equivalent to the crank angle q_C and therefore is also known. Using algebraic manipulations, these equations are transformed into the form of Equation (7). We select the "elbow-up" configuration of the rocker as the solution to find angles ϕ_2 and ϕ_5 .

Given ϕ_5 and q_{FL} , it is straightforward to solve for the spindle position x_{SP} . The loop j_6 - j_7 - j_8 closure is guaranteed by projecting l_5 onto the planes as in Equation (6) and ensuring its length is constant.

4.4.2 Wing constraints. Similarly, B2's armwing constraints define the nonlinear map

$$\mathcal{G}_{\text{wing}} : (x_{SP}, \mathcal{P}) \mapsto (q_{RP}, q_{FE}, q_{AA}) \quad (10)$$

The spindle position x_{SP} and choice of \mathcal{P} determine the armwing angles q_{RP} , q_{FE} , and q_{AA} . This mapping can, in fact, be solved analytically by considering the moving lower triangle mechanism and the upper four-bar linkage.

The mapping $\mathcal{G}_{\text{mech}}$ is derived by imposing constraints that the kinematics must satisfy. These require that loops made by p_1 - p_2 - p_3 and p_2 - p_4 - p_5 - p_6 , as shown in Figure 4, are always closed. For the lower triangle in which x_{SP} drives the mechanism, the vector equation is given by

$$\vec{p_1p_2} + \vec{p_2p_3} + \vec{p_3p_1} = 0 \quad (11)$$

These vectors can be written in two dimensions using rotation matrices to provide the orientation of the length vectors as

$$\text{Rot}_z(q_{RP}) \begin{bmatrix} h_1 \\ 0 \end{bmatrix} + \text{Rot}_z(q_{RP} + q_{FE}) \begin{bmatrix} -r_1 \\ 0 \end{bmatrix} + \begin{bmatrix} -x_{SP} \\ o_2 \end{bmatrix} = 0 \quad (12)$$

The term Rot_z denotes the rotation matrix about the z axis. The four-bar linkage of the rectangle of B2's forelimb can similarly be solved. The loop equation is written

$$\overrightarrow{p_2p_4} + \overrightarrow{p_4p_5} + \overrightarrow{p_5p_6} + \overrightarrow{p_6p_2} = 0 \quad (13)$$

This relation can be written as

$$\begin{aligned} & \text{Rot}_z(q_{\text{RP}} + q_{\text{FE}}) \begin{bmatrix} r_2 \\ 0 \end{bmatrix} + \text{Rot}_z(q_{\text{RP}} + q_{\text{FE}} + q_{\text{AA}}) \begin{bmatrix} c \\ 0 \end{bmatrix} \\ & + \text{Rot}_z(q_{\text{RP}} + \psi) \begin{bmatrix} -r_s \\ 0 \end{bmatrix} + \text{Rot}_z(q_{\text{RP}}) \begin{bmatrix} -h_2 \\ 0 \end{bmatrix} = 0 \end{aligned} \quad (14)$$

The angles q_{RP} and q_{FE} are found by solving the triangle linkage, leaving q_{AA} and ψ as the only unknown angles.

The kinematic loop equations (12) and (14) can be solved analytically to give the solution to the configuration variable \mathcal{Q} . Given values for x_{SP} , and q_{FL} and q_{DV} , the angles q_{RP} , q_{FE} , and q_{AA} are determined from the solution to the loop equations. It should be noted that the configuration variables q_{RP} , q_{FE} , and q_{AA} are wrapped to the interval $[-\pi, \pi]$. This is simply for plotting purposes and is not necessary for accurate computation.

4.5. Forward kinematics

Given the solutions to the constraint equations, it is possible to compute marker positions. There are 14 points on each wing that correspond to origins of links, ends of links, and intersections between links as shown in Figure 4. A detailed explanation of marker selection for comparison with the biological bat is provided in Section 5. The shoulder coordinate frame \mathcal{F}_s has origin at O , and its x and y axes point towards the head of B2 and to the left as shown in Figure 4. The humerus frame \mathcal{F}_h likewise has origin at p_1 and its x axis is aligned with the humerus. The x axis of the radius frame \mathcal{F}_r is set along the radial links with origin p_2 , and the x axis of the carpal frame \mathcal{F}_c is along the carpal plate at p_4 . The three digital frames \mathcal{F}_{di} have x axes aligned with each digit and have origins at p_5 . The hindlimb frame \mathcal{F}_1 has the x attached along the hindlimb. The configuration variable and physical parameters can be used to solve the following forward kinematic equations

$$\begin{cases} [\hat{\mathbf{p}}_1]_{\mathcal{F}_s} = [0 \quad o_1 + o_2 \quad 0]^T \\ [\hat{\mathbf{p}}_i]_{\mathcal{F}_s} = [\hat{\mathbf{p}}_1]_{\mathcal{F}_s} + \text{Rot}_x(q_{\text{FL}})\text{Rot}_z(q_{\text{RP}})[\hat{\mathbf{p}}_i]_{\mathcal{F}_h} \\ \quad i \in \{2, 6\} \\ [\hat{\mathbf{p}}_i]_{\mathcal{F}_s} = [\hat{\mathbf{p}}_2]_{\mathcal{F}_s} + \text{Rot}_x(q_{\text{FL}})\text{Rot}_z(q_{\text{RP}} + q_{\text{FE}})[\hat{\mathbf{p}}_i]_{\mathcal{F}_r} \\ \quad i \in \{3, 4\} \\ [\hat{\mathbf{p}}_5]_{\mathcal{F}_s} = [\hat{\mathbf{p}}_4]_{\mathcal{F}_s} + \text{Rot}_x(q_{\text{FL}})\text{Rot}_z(q_{\text{RP}} + q_{\text{FE}} + q_{\text{AA}})[\hat{\mathbf{p}}_5]_{\mathcal{F}_c} \\ [\hat{\mathbf{p}}_i]_{\mathcal{F}_s} = [\hat{\mathbf{p}}_5]_{\mathcal{F}_s} + \text{Rot}_x(q_{\text{FL}})\text{Rot}_z(q_{\text{RP}} + q_{\text{FE}} + q_{\text{AA}} + \gamma_j)[\hat{\mathbf{p}}_i]_{\mathcal{F}_{dj}} \\ \quad i \in \{7, 8, 9, 10, 11, 12\}, j \in \{1, 2, 3\} \\ [\hat{\mathbf{p}}_{13}]_{\mathcal{F}_s} = [-b \quad 0 \quad 0]^T \\ [\hat{\mathbf{p}}_{14}]_{\mathcal{F}_s} = [\hat{\mathbf{p}}_{13}]_{\mathcal{F}_s} + \text{Rot}_z(\gamma_4)\text{Rot}_y(q_{\text{DV}})[\hat{\mathbf{p}}_{14}]_{\mathcal{F}_1} \end{cases} \quad (15)$$

The Cartesian position vectors of B2's markers with respect to the shoulder frame in the form $[\hat{\mathbf{p}}_i]_{\mathcal{F}_s} = [x_i \quad y_i \quad z_i]^T$ will for the remainder of this article be expressed as $\hat{\mathbf{p}}_i$ to simplify notation. It should be noted that the position vector $\hat{\mathbf{p}}_3$ of spindle marker p_3 is restricted to motion along the x axis of the body frame because of the constraints of the mechanism.

5. Optimization

The parametric model derived in Section 4 provides a clear relationship of the selected actuator trajectories \mathcal{Q}_a and the physical parameters \mathcal{P} to the positions of the markers on B2. In this section, we address the selection of values for \mathcal{Q}_a and \mathcal{P} . The primary objective of this article is to provide the closest matching of B2's kinematic synergies to those of the biological bat. Identifying the appropriate values for \mathcal{Q}_a and \mathcal{P} gives a solution to this goal. Yet, this proves challenging because there exists a difference in topology between the skeletons of B2 and the biological bat. Furthermore, B2 has only three DoAs compared with the >40 DoFs in a biological bat.

This section presents a method for optimizing the values for \mathcal{Q}_a and \mathcal{P} such that the calculated synergies of B2 most closely match those of a biological bat. The synergies of B2 are derived from the Euclidean positions of the points on its wing, and likewise those of the biological bat are determined from markers painted on the wing and tracked with high-speed cameras. This method for selecting actuator trajectories and parameter values is formulated as an optimization problem. We describe in detail each step of the optimization and outline the cost function.

5.1. Marker selection for comparison

To match the synergies of B2 to those of a biological bat, it is necessary to consider how to compare these two systems. As described in Section 3, Riskin et al. (2008) presented an experiment in which marker placement was determined to best characterize the dimensional complexity of a biological bat. It used 17 markers to capture this dimensional complexity of over 20 DoFs in one wing. Compared with this biological bat, B2 has a significantly reduced complexity, with only three actuators contributing three DoAs to the system for this new design. Furthermore, there are major topological differences between the skeletal structures of a biological bat and B2. The forelimb mechanism of each wing of B2 contains extra linkages that constrain it to one DoF. These differences preclude exact replication of the movements and kinematics of a biological bat in B2.

Careful consideration of the similarities between B2 and the biological bat is thus necessary to produce meaningful comparisons between the two for successful optimization results. Marker selection was performed as in Hoff et al. (2016). B2 has markers on the shoulder, elbow, wrist, three wingtips, hip, and ankle that correspond well to equivalent markers on the biological bat. The shoulder marker

matches marker p_1 on B2. Likewise, the elbow and wrist have the equivalent markers p_2 and p_4 on B2. The bat's three wingtips paired with B2's wingtips p_{10} , p_{11} , and p_{12} , and the hip and ankle with p_{13} and p_{14} . However, B2 lacks joints on its digits that are present in the biological bat, which has two joints on each of the three digits. These markers on the biological bat were omitted. The sternum markers on the bat were also not matched to B2, but they were used to define the body-referenced coordinate frame of the biological bat.

The motion capture data of these chosen markers (of the form $\mathbf{p}_i = [x_i \ y_i \ z_i]^\top$ for one wingbeat cycle) of the biological bat were combined into a matrix with identical format as Equation (1) but with $n_p = 8$ markers instead of 17 markers. Likewise for B2, for a set of choices of \mathcal{Q}_a and \mathcal{P} over a wingbeat cycle, the forward kinematics in Equation (15) in turn with the projection of the biological bat markers produce the marker positions for each instance in time, and the data can be similarly compiled into the matrix with the same form as Equation (1) for the $n_p = 8$ selected markers.

5.2. Constrained optimization formulation

The forward kinematics equations given by Equation (15) establish the relationship of the configuration variables and physical parameters to the positions of the markers on B2 when the constraints in Section 4 are satisfied. Using this map, the trajectories of B2's markers can be compared with those of the biological bat. This comparison can be quantified as a cost function that penalizes B2 for deviating from the movement of the biological bat. A constrained optimization problem is then formulated such that the minimizing variables are the trajectories of the actuated coordinates \mathcal{Q}_a and the physical parameter vector \mathcal{P} .

However, not all of the parameters that describe the structure of B2 can be changed. It is unnecessary to optimize for r because this parameter can simply be absorbed into each of the digit lengths d_1 , d_2 , and d_3 . Changing r would not affect the length of the digits. The two offsets o_1 and o_2 are fixed parameters and thus cannot be optimized. The hindlimbs of the biological bat are not being considered because they are significantly smaller than those of B2. Hindlimbs this small fail to stabilize B2. Thus, the body length b , the angle γ_4 on the hindlimb, and the length of the hindlimb l are not optimized. The 12 optimized parameters h_1 , h_2 , r_1 , r_2 , r_3 , c , d_1 , d_2 , d_3 , γ_1 , γ_2 , and γ_3 are combined into the vector $\bar{\mathcal{P}}$. The parameters \mathcal{C} for the coupling mechanism have been tuned by hand such that the spindle trajectory $x_{SP}(t)$ closely matches the ideal trajectory were the spindle allowed free range of motion in the optimization, i.e., if x_{SP} was directly actuated and optimized for as presented in the methods of Hoff et al. (2016).

The trajectory of the crank angle is parameterized by an angular frequency ω and a phase shift ϕ as

$$q_C(t_i) = \omega t_i + \phi \quad (16)$$

A brushless DC motor connected by a set of gears drives the crank at some fixed throttle, and this throttle is a mapping to the frequency ω . These parameters are grouped into the vector $\mathcal{A}_C = [\omega \ \phi]^\top$. The hindlimb trajectory $q_{DV}(t)$ is not optimized because the hindlimbs are used for control in flight, and thus tracking biology in this case would lead to instability.

The optimization process is separated into two routines. The set of trajectory coefficients \mathcal{A}_C and the structural parameters $\bar{\mathcal{P}}$ are optimized individually using Matlab's constrained optimization algorithm *fmincon* with an interior-point algorithm. For a given routine, the variable to be optimized is expressed as $\mathcal{X} \in \{\mathcal{A}_C, \bar{\mathcal{P}}\}$. First, the optimized variable is selected to be $\mathcal{X} = \mathcal{A}_C$ to find the coefficients for the crank trajectory. Given the values for q_C and \mathcal{C} , Equations (7) and (9) provide analytical solutions to the spindle position q_{FL} and the flapping angle x_{SP} . Equations (12) and (14), those mathematically describing the constraints of the forelimb mechanism, are solved to find \mathcal{Q} . From this, the forward kinematics in Equation (15) can be computed to find B2's marker positions. These positions at each instant in time over a wingbeat cycle are grouped together to form the data matrix $\hat{\mathcal{M}}$. PCA is then performed to acquire the first two principal components of the given iteration from this generated data. PCA is only performed once on the biological data, outside of the optimization routine, because it is independent of the optimizing variables. The cost function \mathcal{J} (defined in the following section) is computed from these values.

The routine for $\bar{\mathcal{P}}$ is then successively run. The routine is identical except that the variable being optimized is changed and the constraints slightly differ. This sequence of consecutively running the optimization routines is iterated until a converging solution is reached. About four iterations have shown to be adequate. Furthermore, we have run tests for various initial conditions of both the structure and the crank trajectory. When the initial conditions for the structure are a feasible configuration, i.e., one that can be actuated without singularities, the optimization converges to a common solution with minimal variation.

5.3. Cost function

It is important to define a mathematical space in which the principal components between B2 and the biological bat can be matched. The most obvious choice is to directly minimize the 2-norm of the difference between principal components. However, the principal components alone are a set of eigenvectors and emphasize the dominant directions of motion. They say nothing about the temporal component of the spatiotemporal data. The temporal component is described by the projection of the original data onto its set of principal components, also known as the principal component score. The projection shows the weights of the principal components over the wingbeat cycle, or the importance of the principal components over the time period. The formulation presented here compares the data

between B2 and the biological bat after performing PCA and reconstructing the data. This incorporates both the principal components as well as their projections.

Reconstruction via PCA is formulated as follows. The matrix \mathcal{M}_r refers to the reconstruction after dimensionality reduction from PCA on the biological bat data \mathcal{M} . Matrix $\hat{\mathcal{M}}_r$ is similarly generated from the simulated B2 data $\hat{\mathcal{M}}$. Only the steps for finding \mathcal{M}_r are included because the procedure is identical for finding $\hat{\mathcal{M}}_r$. First, mean subtraction is performed to make each column of \mathcal{M} to have zero mean. This can be quantified as

$$\mathcal{M}_c = \mathcal{M} - \mathbf{1}_n \boldsymbol{\mu}^\top \quad (17)$$

The term $\mathbf{1}_n$ is a column vector of ones with length n , i.e., the number of time samples. The term $\boldsymbol{\mu}^\top = [\mu_1 \ \mu_2 \ \dots \ \mu_{3n_p}]$ represents the sample mean of the xyz coordinates of the markers over all the time samples, i.e., the mean of the columns of matrix \mathcal{M} . Variable μ_1 is the mean of the x coordinate of \mathbf{p}_1 over all t , μ_2 is the mean of the y coordinate of \mathbf{p}_1 , and so on.

Next, singular value decomposition (SVD) is applied to the mean-centered matrix \mathcal{M}_c giving

$$\mathcal{M}_c = \mathcal{U} \boldsymbol{\Sigma} \mathcal{V}^\top \quad (18)$$

The data matrices are formatted such that $\mathcal{V} = [\mathbf{v}_1 \ \mathbf{v}_2 \ \dots \ \mathbf{v}_{3n_p}]$ contains the principal components. Thus, the j th column of \mathcal{V} is the component \mathbf{v}_j . In addition, the matrix $\mathcal{U} \boldsymbol{\Sigma} = [\mathbf{u}_1 \sigma_1 \ \mathbf{u}_2 \sigma_2 \ \dots \ \mathbf{u}_{3n_p} \sigma_{3n_p}]$ represents the temporal weights of the principal components over the wingbeat cycle, with the weight vector \mathbf{u}_i as the i th column of \mathcal{U} , and singular value σ_i as the i th diagonal element of $\boldsymbol{\Sigma}$. We then perform dimensionality reduction by setting all except the first two singular values of $\boldsymbol{\Sigma}$ equal to zero such that only the first two principal components \mathbf{v}_1 and \mathbf{v}_2 are used to reconstruct the data. Using the mean of the data matrix and the first two principal components, the data can be reconstructed with the reduced order matrices given by

$$\mathcal{M}_r = \mathbf{1}_n \boldsymbol{\mu}^\top + \mathbf{u}_1 \sigma_1 \mathbf{v}_1^\top + \mathbf{u}_2 \sigma_2 \mathbf{v}_2^\top \quad (19)$$

The mean is removed from the original matrix prior to SVD, so it is added in reconstruction as $\mathbf{1}_n \boldsymbol{\mu}^\top$. The reconstructed data for B2 is similarly derived. The matrices \mathcal{M}_r and $\hat{\mathcal{M}}_r$ will be in the same format as Equation (1), but the vectors $\mathbf{p}_i(t)$ and $\hat{\mathbf{p}}_i(t)$ are replaced with the terms $\mathbf{p}_{r,i}(t)$ and $\hat{\mathbf{p}}_{r,i}(t)$. These denote the reconstructed marker positions. Both matrices will have at most rank 3. The mean, the first principal component, and the second principal component each contribute one dimension.

Repetitions of the optimization procedure indicated that there was little improvement in the minimum value computed for the cost function when increasing the number of principal components to more than two. Using more than only the two most dominant principal components was redundant.

Given the matrices $\hat{\mathcal{M}}_r$ and \mathcal{M}_r , the optimization of B2 over a wingbeat cycle is formulated as

$$\begin{aligned} & \underset{\mathcal{X}}{\text{minimize}} && \mathcal{J}(\mathcal{X}) = \left\| \hat{\mathcal{M}}_r(\mathcal{X}) - \mathcal{M}_r \right\|_F^2 \\ & \text{subject to} && f_1 : \gamma_1 \leq \gamma_2 \leq \gamma_3 \\ & && f_2 : l_k \leq \bar{\mathcal{P}}_k \leq u_k, \quad k = 1, \dots, 12 \\ & && g_1 : q_C(t_1) - q_C(t_n) \in \{0, \pm 2\pi, \dots\} \end{aligned} \quad (20)$$

The notation for this equation will be described in the following paragraphs. The variable being optimized is $\mathcal{X} \in \{\mathcal{A}_C, \bar{\mathcal{P}}\}$ such that each is optimized separately in its own routine as described above. The matrix $\hat{\mathcal{M}}_r$ is dependent on the optimization variable \mathcal{X} because its changing values will affect the marker positions of B2.

The objective function \mathcal{J} implements the sum of squared differences between the Euclidean positions of the markers B2 and the biological bat that are reconstructed from the mean and the first two principal components. Thus, the function is written as the Frobenius norm, which is given by

$$\|A\|_F^2 = \sum_{i=1}^n \sum_{j=1}^m |a_{ij}|^2, \quad A \in \mathbb{R}^{n \times m} \quad (21)$$

where a_{ij} is the element in the i th row and j th column of matrix A . These marker positions are reconstructed from the two most dominant principal components, and thus matching the reconstructed markers of B2 to those of the biological bat will embed the synergies found in the bat into B2.

The inequality constraint f_1 prevents the digits of B2 from overlapping with each other in the optimization. The second constraint f_2 sets upper and lower bounds on the structural parameters. The term $\bar{\mathcal{P}}_k$ refers to the k th element of $\bar{\mathcal{P}}$, and these elements are restricted to a range with the lower and upper bounds l_k and u_k on the optimization of the structural parameters. In particular, the digit angles γ_1 , γ_2 , and γ_3 are restricted to the range $[-\pi, \pi]$. The values for h_1 , h_2 , r_1 , r_2 , r_s , and c have feasible limitations for their lower bounds. The structure would be impossible to construct for too small of values because joints and parts would overlap. Lower bounds were chosen appropriately based on the structural limitations. The upper bound for each was selected to be the wingspan $B_{R.a.}$ of *Rousettus aegyptiacus* (Norberg, 1972; Norberg and Rayner, 1987). This is beyond any reasonable size for these links and, thus, provides freedom for the optimizer while also reducing the search space to improve computation time. The three digit lengths were allowed to decrease to length 0, and were restricted from lengths above that of the longest digit of *Rousettus aegyptiacus* (Norberg, 1972). This prevents B2 from having abnormally long digits and a small forelimb structure. The equality constraint g_1 is given to ensure the periodicity of the crank cycle. Mathematically speaking, the crank should start and end at the same angle wrapped to the interval 2π .

6. Results

In this article, we claim that mimicking biology more closely through a second stage of design of a robot can improve the robot's performance. Specifically, for the case of B2, we have optimized the kinematic synergies of its wings to match those of a biological bat with motion capture data. We validate B2's matching of biology through simulation results and motion capture experiments, and we show an improvement in performance through lift force measurement tests on a load cell. Flight results demonstrate that this new design does not induce unstable modes in B2's orientation. The simulation results of the optimization routine give the new wing structure with optimized geometric parameters as well as the actuator trajectories of B2 that best replicate the synergies of the biological bat. We compare the biologically meaningful angles q_{FL} , q_{RP} , q_{FE} , and q_{AA} in B2 and the biological bat as well as their two most dominant principal components. The simulation results are verified in experiment in which the optimized structure of B2 is assembled and tested. B2's kinematics are recorded in Vicon motion capture experiments, and the results are compared to simulation results and the biological bat data. Load cell results measuring lift force production substantiate our claim of improved performance by comparing the new mechanism's activation of the folding–unfolding synergy within a wingbeat case to the case when the wings are fixed in the outstretched position. B2's resulting behavior in both simulation and experiments closely matches biology, and there are significant lift production improvements as a result of the folding–unfolding of the wings within a wingbeat.

6.1. Simulation

The performance of the optimization routine can be evaluated by the similarity of the resulting two dominant principal components in the biological bat and B2. These components are eigenvectors, and they form a basis in which the markers on B2 and the biological bat are defined. Figure 6 displays the similarity between the two sets of principal components. The variable number refers to the Cartesian coordinate of a given marker, and the weight determines its value. A principal component gives the direction of motion of each data marker, and a linear combination of all of the principal components added to the mean marker positions reproduces the actual positions of the markers. The reconstructed motion of the points can be determined using the principal components and their weights over time.

The resulting decision parameters from the optimization routine that yield these principle components are the trajectories of the actuated coordinates Q_a and the values for the physical parameter vector $\bar{\mathcal{P}}$. These new physical parameters are compared against the values of the original prototype in Table 1 and Figure 7. There are changes in the placement and lengths of the three digits as well as the

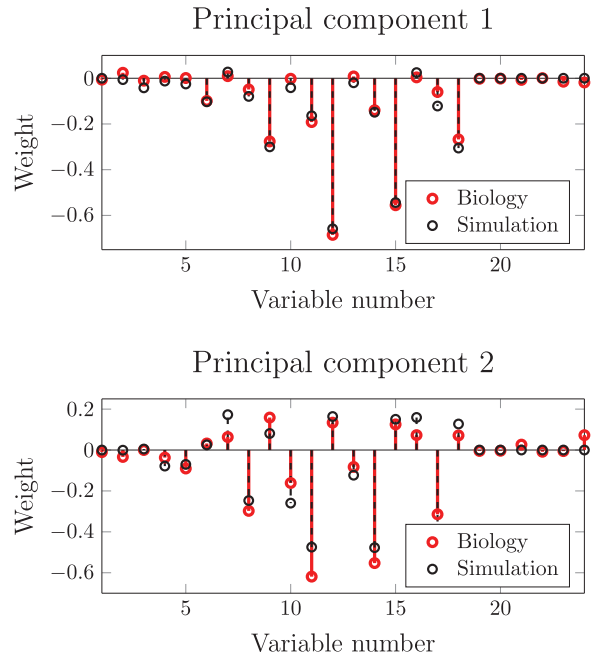


Fig. 6. Principal components 1 and 2 of the biological bat (red) and B2 (dotted black). For biology, the first principal component is column 1 of matrix \mathcal{V} , and the second is column 2. This is the same for B2 in matrix $\hat{\mathcal{V}}$.

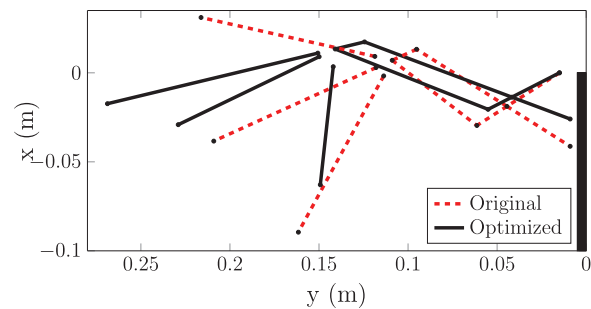


Fig. 7. Original prototype structure (dotted red) of B2 versus the resulting structure (black) after running optimization.

linkages that affect the mechanism's kinematic behavior. Direct comparison of these to biology, however, is not as informative because of the topological differences in structure between the wings of B2 and the biological bat. The crank trajectory q_C and B2's new parameters by themselves do not offer a meaningful comparison. Therefore, we consider the resulting joint evolution of the biologically meaningful angles in B2 that are produced as a result of the selection of these decision parameters and compare these with biology.

These angles in B2 over a wingbeat cycle were calculated via simulation and are compared with those of the biological bat in Figure 8. Both B2 and the biological bat have a flapping frequency of 8 Hz, giving a wingbeat period of 0.125 s. Only one wingbeat cycle is shown in the results. In this figure, we have presented the angles with their offsets removed. This is calculated as

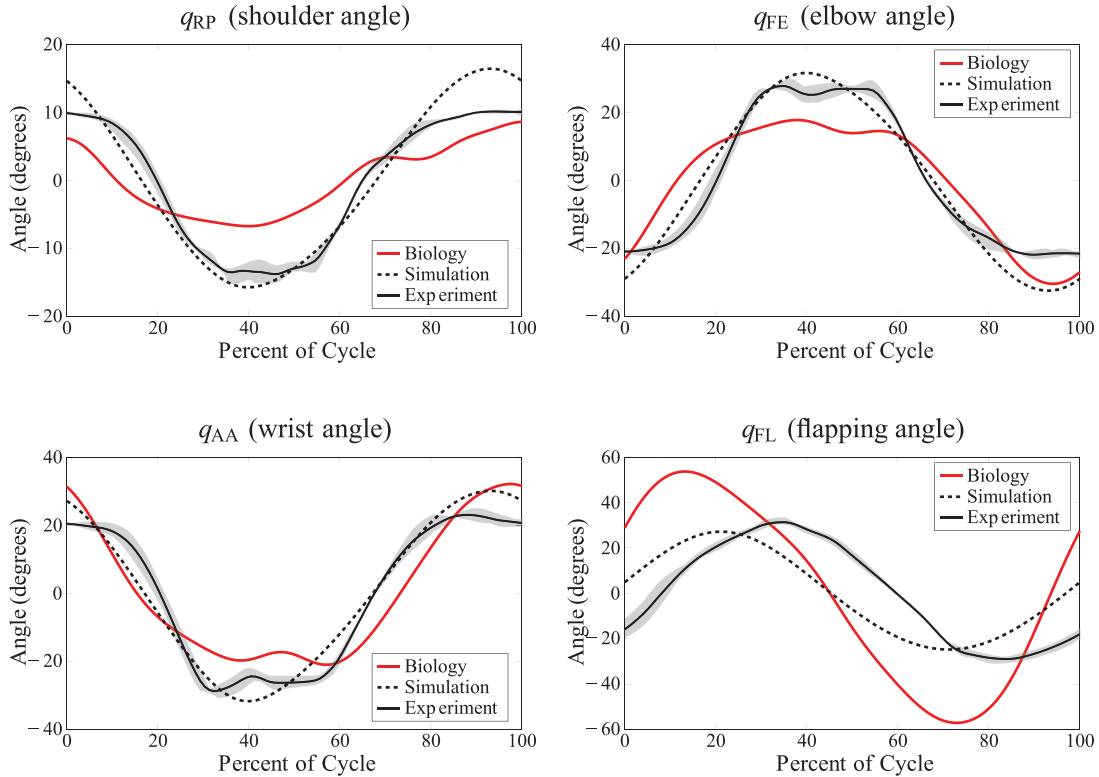


Fig. 8. Comparison of the trajectory results of one wingbeat cycle of biologically meaningful angles of the biological bat (red), the simulation of B2 (dotted black), and the experimental results of B2 from four Vicon motion capture tests (solid black with gray outline). The gray shading is the range between the maximum and minimum values of the four tests with frequencies between 3.5 and 5 Hz, and the solid black line is the mean of these tests. In each plot, the angle offsets have been removed by subtracting the mean angle position over the period from each sample such that each angle is centered about the origin. B2's angles q_{RP} , q_{FE} , and q_{AA} are coupled in their motion, and they depend solely on the spindle position x_{SP} . The flapping angle q_{FL} is driven by the crank. With the coupling mechanism engaged, the system reduces to one DoF. The crank angle q_C will drive x_{SP} , and resultantly these four biologically meaningful angles are coupled.

$$q_i^c(t) = q_i(t) - \bar{q}_i, \quad \bar{q}_i = \frac{1}{n} \sum_{t=1}^n q_i(t) \quad (22)$$

where q_i is the choice of $\{q_{RP}, q_{FE}, q_{AA}, q_{FL}\}$, \bar{q}_i is the mean of $q_i(t)$ over the period, and $q_i^c(t)$ is the mean-centered angle. We center the angles because the structural topology of B2 is fundamentally different from biology; it included extra linkages not present in biology. The absolute angles on these two structures are not as informative for comparing the evolution of their joints. Centering allows comparison of the changing behavior of the joint angles over the wingbeat period.

As seen in the figure, B2's resulting wingbeat period includes folding–unfolding of the wings as well as the vertical flapping motion of the wings similar to a biological bat in straight flight. The elbow and wrist angles q_{FE} and q_{AA} track biology very accurately. The amplitude of B2's flapping angle q_{FL} is lower than that of the biological bat. Structural and actuator limitations prohibit this large of a flapping amplitude to be implemented in hardware. If the crank radius r_c were to be lengthened to increase flapping amplitude, the system nears

mechanical singularities because the drive link l_1 reaches configurations close to parallel with the shoulder and lockups occur. The shoulder angles q_{RP} have different amplitudes because of the difference in mechanical advantages between B2 and biology. B2's armwing mechanism was designed to have a large mechanical advantage to lower the torque load on the motor, and as a result the spindle x_{SP} moves a relatively longer distance to produce the wing folding–unfolding. This, in turn, results in a large amplitude of q_{RP} .

The coordinated motion of flapping and folding of the wings can be observed in Figure 8. The actual marker trajectories of the three wingtips of both biology and simulation are plotted. While B2's flapping amplitude is smaller than biology, its synchronization of flapping and folding have the same distinct pattern as biology. The wings begin to extend toward the end of the upstroke portion of the wingbeat period, and they reach full extension during the downstroke. Like biology, the wings then retract in preparation for the upstroke. B2 demonstrates this properly timed synchronization of flapping and folding despite only having one DoA driving the wings.

Table 1. B2's morphological dimensions. The optimized parameters are the results when the coupling mechanism is used.

Parameter	Original	Optimized	Unit
h_1	3.5	3.0	cm
h_2	2.0	1.5	cm
r_1	4.2	3.5	cm
r_2	6.0	8.8	cm
r_s	6.0	9.2	cm
c	1.5	1.7	cm
d_1	10.0	12.2	cm
d_2	10.0	8.8	cm
d_3	10.0	6.7	cm
γ_1	-37.0	0.0	°
γ_2	0.0	12.2	°
γ_3	37.0	70.2	°

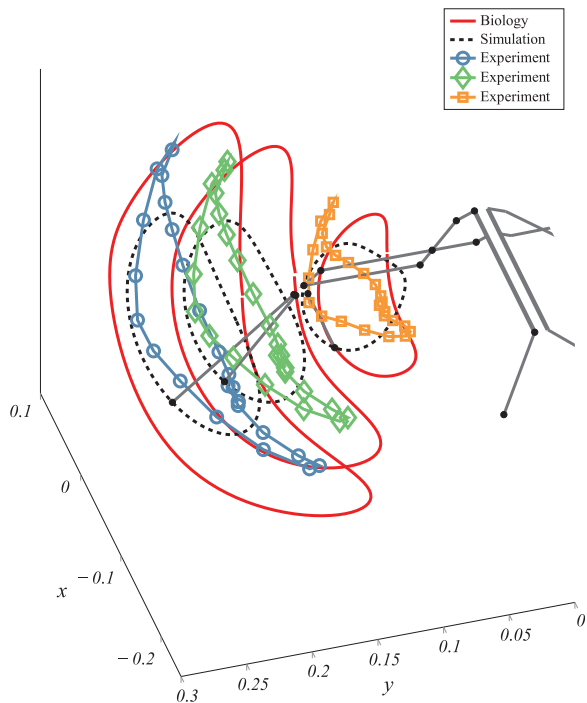


Fig. 9. Wingtip marker trajectory comparisons of the biological bat (red) and B2 in simulation (dotted black) and motion capture experiments (blue, green and orange) for one wingbeat period.

6.2. Experiments

We constructed B2 with the optimized parameters from Table 1, and the robot prototype is displayed in Figures 3 and 10. Carbon fiber rods were used for parameters h_1 , r_1 , r_2 , r_s , d_1 , d_2 , d_3 , and h_1 . The parameters h_2 and c were included in the dimensions of 3D printed parts. The fuselage consists of two carbon fiber plates secured to each other with nylon screws and plates. We replaced the carbon fiber shoulder plates with aluminum plates (h) to minimize structural deformations when the system was flapping. Thrust axial bearings (a) in each of the armwing joints

reduce friction and allow for smooth folding of the wings. A BLDC motor (g) is attached to the pinion gear (f) to power the gearbox (e), (d) in between the fuselage plates. Metal collars (i) hold the gearbox in place. The crank arms are tightened to the crankshaft with set screws, and their ends connect to the shoulder with ball-and-socket joints (b) and a threaded rod.

We built the coupling mechanism with 3D printed parts and ball-and-socket joints. Two ball-and-socket joints (c) fixed together by a threaded rod connect the crank arm to the 3D printed rocker arm. This arm is similarly connected to the slider with two ball-and-socket joints. We minimized slider friction by inserting a Teflon tube in the 3D printed part that is constrained to the stainless steel rod that replaced the spindle. Finally, we secured a compliant silicone membrane to the wings, hindlimbs, and body. The membrane's flexibility allows for the changing wing area over a wingbeat. Excess tension inhibits actuation.

6.3. Motion capture

The simulation results from the optimization can be verified experimentally by measuring the kinematic behavior of the optimized prototype. We developed an experiment to record the equivalent marker positions of the prototype over a full wingbeat period in order to examine the agreement of the biologically meaningful angles between simulation and the prototype. We attached reflective markers to the shoulder (p_1), elbow (p_2), wrist (p_4), wingtips (p_{10} , p_{11} , p_{12}), hip (p_{13}), and ankle (p_{14}) of B2 such that the biologically meaningful angles q_{RP} , q_{FE} , q_{AA} , and q_{FL} could be calculated. Each marker was attached on top of B2's left wing.

We secured B2 onto a stable platform in the middle of eight Vicon T40 motion capture cameras in the Intelligent Robotics Laboratory (IRL) flight arena at the University of Illinois in Champaign-Urbana. A 2S LiPo battery powered B2's BLDC to generate the flapping and folding-unfolding in each experiment. We left the membrane attached to B2's skeleton to be consistent with the other experimental results. The Vicon Tracker 3.4 software coordinated the cameras to track the marker locations and output 3D position data from an inertial frame of reference with origin in the center of the arena. We utilized the Vicon DataStream SDK to collect the 3D Cartesian position of each marker at a frame rate of 100 Hz. We recorded four test with each at a different throttle input to the motor to characterize the kinematics over a range of wingbeat frequencies from 3.5 Hz to 5 Hz.

We changed the coordinate system from the inertial reference frame to the body frame to match B2's simulations and the biological data. We present the results of the motion capture experiments in the same manner as the biological data and simulation results. The resulting angle trajectories of B2 are compared in Figure 8. Figure 9 gives the comparison of the motion capture position data of the markers between biology, simulation, and the motion capture results.

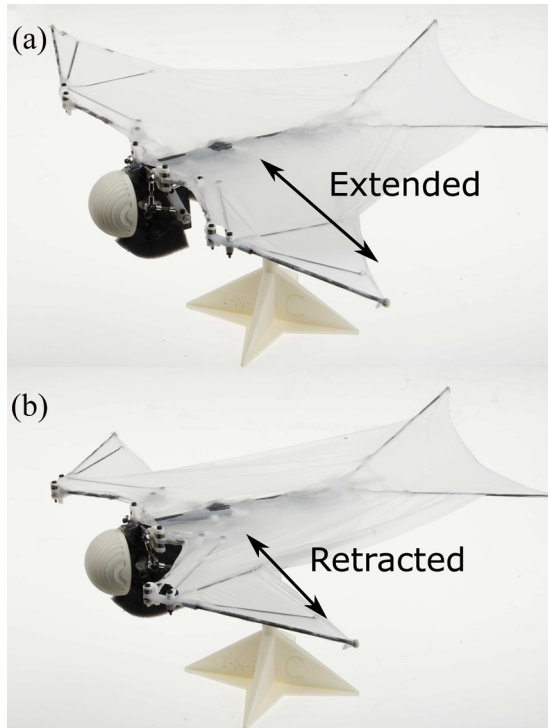


Fig. 10. A: Optimized B2 prototype with wings at full extension. B: Optimized B2 prototype with wings fully retracted.

From each of these plots, it can be seen that the experimental motion capture results match closely with simulation. The angle trajectories of q_{RP} , q_{FE} , and q_{AA} in Figure 8 have nearly identical behavior to those of B2 in simulation. The angles in each of the tests have been centered with Equation (22) to provide comparison with biology. There is a phase shift between simulation and experiment for the angle q_{FL} , and this can be explained by the rigid set of linkages that drive flapping and folding. These motions are slaves to the crank, and the different latencies in each of the responses of flapping and folding explain this phase shift. In addition, q_{FL} from the motion

capture data has a larger amplitude. This is seen in both Figure 8 and in the wing marker trajectories of Figure 9. The wings consist of carbon fiber rods that are flexible. The wing inertia during flapping causes these rods to bend, slightly increasing the measured wing amplitude. This is most pronounced for the wingtip marker trajectories in Figure 9.

6.4. Load cell

In biological bats, it is thought that wing folding during the upstroke reduces the cost of flight because of the lower wing inertia and drag (Riskin et al., 2012). Bahlman et al. (2013) constructed a robotic bat to examine this phenomenon. Similarly, we sought to characterize the performance improvements because matching the synergies of biology resulted in wing folding during the upstroke. We studied the effects that more closely matching biological synergies had on flight performance by conducting load cell experiments to measure lift production.

B2 was mounted on an analog six-axis JR3 force-torque sensor (model #30E12A4). A dSPACE CLP1104 I/O box recorded the signals from the load cell, and these were saved on a desktop computer with a DS1104 R&D Controller Board. The signals were sampled at a frequency of 1000 Hz. We secured B2 to a carbon fiber rod that protruded from the top of the load cell. A power supply set at a fixed voltage of 8.4 V powered a speed controller that drove the BLDC motor.

To show lift improvements of the optimized design, we considered the two cases of flapping with the coupling mechanism engaged to produce folding–unfolding within a wingbeat period and flapping with the wings fixed at full extension (coupling mechanism disengaged). We ran experiments in a downstream flow with velocity 3 ms^{-1} . Five tests were recorded for the folding–unfolding case, and five were recorded for the fixed case for 2 seconds per test. In each test, B2 was positioned to have zero angle of attack. To provide consistency in the results, we drove B2

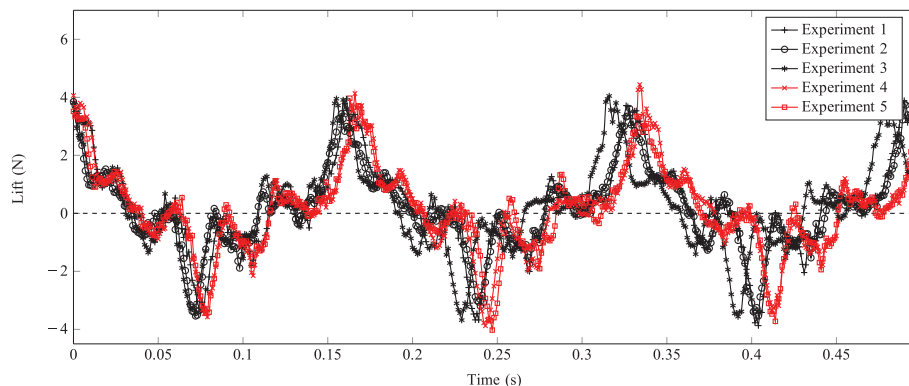


Fig. 11. Load cell experiments measuring the force of lift of B2 when the wings are fixed such that no morphing occurs. Five tests are shown with varying marker styles, each having a frequency of 6 Hz. The average lift of all tests was 0.149 N. The power for each test was 8.4 W.

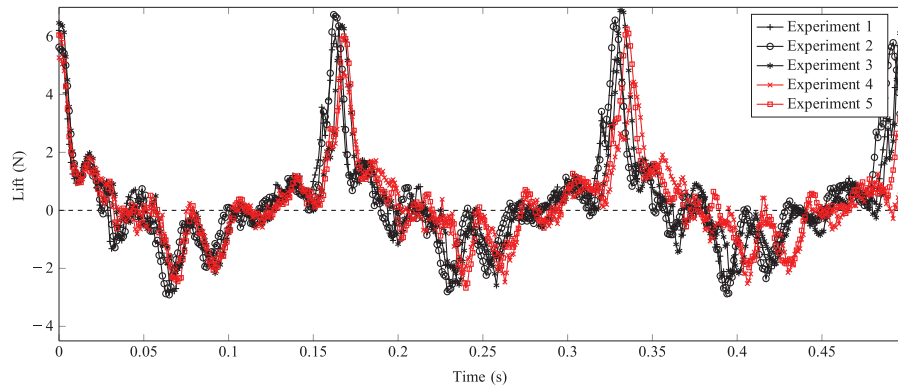


Fig. 12. Load cell experiments measuring the force of lift of B2 when the wings are folding and unfolded within a wingbeat. Five tests are shown with varying marker styles, each having a frequency of 6 Hz. The average lift of all tests was 0.282 N. The power for each test was 10.0 W.

to flap at roughly 6 Hz for all tests. This required an input current of 1.2 A when the wings actively folded and 1.0 A when the wings were fixed at extension. Each test was recorded for 2 seconds.

We likewise collected data for the resting position with no downstream flow to separate lift generation from the total force readings. The raw data consisted of the net force in the z direction of the load cell which pointed up for zero angle of attack. We post-processed the force readings for each test by subtracting the average resting force readings from the test data. The resulting data was the force of lift generated from flapping in the downstream flow.

Figure 11 presents the results of the load cell tests when B2's wings were fixed. We plot the lift of three wingbeat periods for each of the five tests over a 0.5 s interval to show consistency of the measurements over each period. The peak lift reading marked the start of a given test such that the data were aligned properly. Similarly, we present the results for tests when the coupling mechanism was engaged to fold the wings in Figure 12. The wingbeat period is clearly visible in both plots, but there are high-frequency oscillations within these periods that are present in the two plots. B2's wings are relatively heavy with respect to the overall body mass, and the flapping motion produces large inertial forces that cause oscillations about the center of mass.

We can make two significant observations by comparing the results of Figures 11 and 12. First, these plots are in agreement with the hypothesis that a bat's folding of its wings during the upstroke portion of the wingbeat period reduces negative lift (Riskin et al., 2012), and they complement past experiments in robotic bat wing folding that have studied this phenomenon (Bahlman et al., 2013). When a bat folds its wings in the upstroke, both the wing inertia is reduced and the negative lift is reduced. Reducing negative lift is constructive because it results in an overall net lift gain. Clearly, B2's negative lift is reduced when the wings are folded in the upstroke. The lift measurements drop down to around -4 N for fixed flapping, and the readings for folding have minima of about -3 N.

Second, we can conclude that overall lift production is improved. We consider the net generated lift of each trial by computing its average force over the whole 2 seconds of data. This is calculated for each test k as $\bar{F}_{\text{lift}}^k = \frac{1}{N} \sum_{t=1}^N F_{\text{lift}}^k(t)$ where $t=1$ marks the start of the first peak, and $t=N$ is the data point before the last peak. The mean lift of the folding experiments were 0.267 N, 0.241 N, 0.263 N, 0.304 N and 0.333 N, and those for the fixed case were 0.153 N, 0.136 N, 0.136 N, 0.157 N and 0.163 N. The mean over all of these averages with folding engaged is 0.282 N, compared with a mean lift of 0.149 N for the fixed wing tests. This is an 89% improvement in lift production. In addition, the maximum lift value reached over all the folding cases peaks above 6 N whereas the fixed case reaches only 4 N.

One negative aspect of wing folding is that it can be accompanied by a reduction in net thrust (Bahlman et al., 2013). In this case, however, thrust penalties were quite low, with average forward force of 0.007 N less than the fixed-wing case recorded on the load cell. The net forward force includes both thrust and drag components in the x direction. Thus, a net force of 0 N means that B2 would maintain its velocity (the wind speed of the load cell tests), >0 N and its velocity would increase, and <0 N and its velocity would decrease. The average forward force for each test was calculated the same as average lift. The respective averages of the net forward forces of each of the individual trials are 0.004 N, 0.002 N, -0.001 N, -0.015 N, 0.009 N for the folding case and 0.010 N, 0.004 N, 0.011 N, 0.010 N, -0.002 N for the fixed case. The flapping frequency was approximately 6 Hz for all tests. Increasing the frequency would generate more thrust for both cases and eliminate averages that were less than 0 N.

Folding and unfolding of the wings synchronously with flapping draws more current (1.2 A) than fixed wing flapping (1.0 A). The extra torque load of the coupling mechanism driving folding-unfolding is placed on the crank, and thus the motor requires a higher current to generate a given wingbeat frequency. Although this is a negative effect of the added mechanism, it may be the case that B2 can

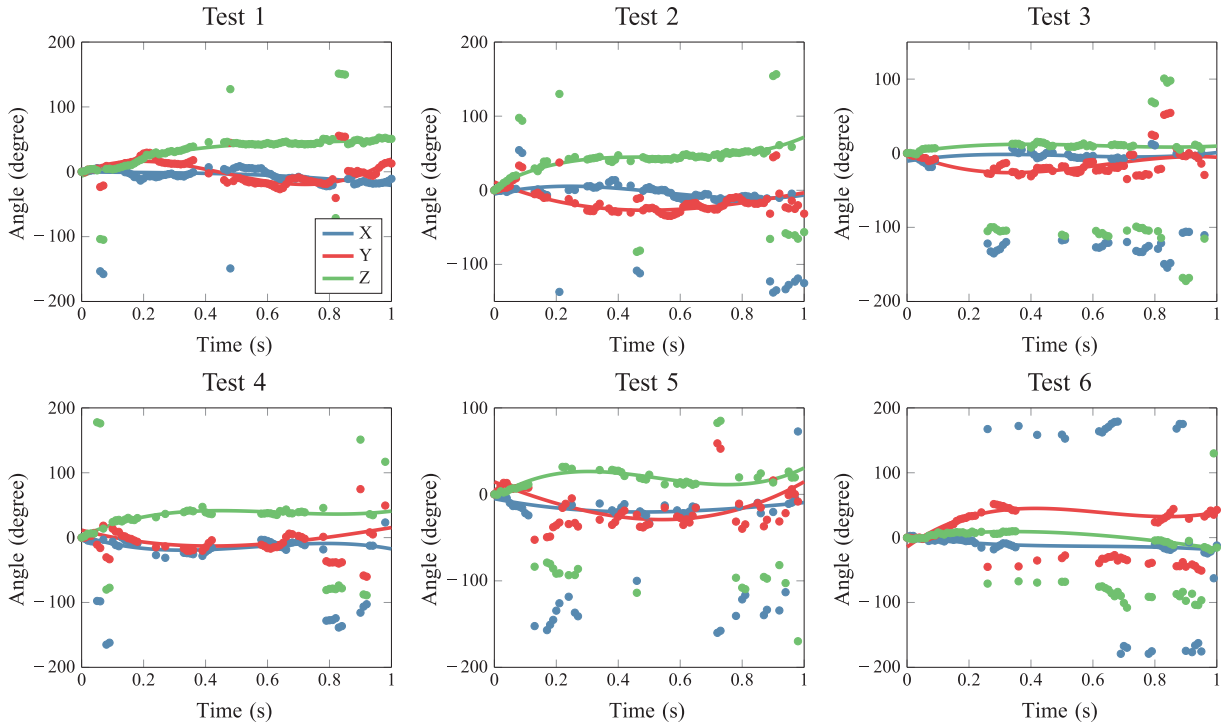


Fig. 13. Orientation of B2 in XYZ Euler angles for six manually launched open-loop flight tests sampled at 100 Hz with the Vicon motion capture system. The flight time of each test is approximately 1s. We fix the inertial frame to be the orientation of B2 at the first time sample, and the Euler angles are measured with respect to this inertial frame. The actual data for each test is plotted with solid markers. The gaps in between markers are occlusions in which no orientation could be determined. The lines are best-fit third-order polynomials to the data points ignoring the outliers in the data. The reflective markers on B2 were relatively close together and occasionally caused the Vicon Tracker 3.4 software to miscalculate orientation, which explains these jumps in the readings.

sustain flight with a lower wingbeat frequency because of these lift improvements. In this case, it is possible that the overall efficiency of the system is improved. However, more extensive testing is necessary to better understand the relationship between thrust, lift, and electrical power before any claims about efficiency can be made, but these analysis are beyond the scope of the works in this article.

6.5. Flight experiments

We performed a series of untethered flight experiments in the IRL flight arena with the newly designed system (Figure 10) to demonstrate that the folding mechanism does not induce unstable flight modes in B2's orientation during flight. This has an open space with a length of about 8 equipped with a Vicon motion capture system to record orientation and foam padding on the ground that protects the robot from damage during flight tests.

We recorded six 1-second long flight tests. We extended the hind limbs by 50% to improve passive stability for these open-loop tests because the on-board sensing was not used in order to reduce weight. B2 was launched manually after initiating the throttle, and its orientation was recorded by tracking four reflective markers extruding from the front of the fuselage. The XYZ Euler angles describing B2's orientation over each flight are shown in Figure 13. We note that

the Vicon system is sensitive during these flights because the reflective markers were spaced closely together: it can be seen from the plots that in each of the angles, the orientation makes discontinuous jumps and in some cases the markers are occluded such that no data points are available. Therefore, we fit third-order polynomials ignoring the occlusions and outliers to show the general behavior of the orientation. It is clear from these figure that, ignoring the discontinuities, each angle is bounded in its response. This supports our observations of each flight test that the synchronous folding and flapping motion does not produce instabilities in the orientation.

In future tests, the on-board computer should be added for closed-loop control. Efforts will also be directed at extending these flight results to longer durations. We may also reintroduce control action that makes asynchronous adjustments to the coupling mechanism on each side to be suitable for extended closed loop flight to compensate for roll instabilities. We will require a controlled environment with more space to perform extended flight tests.

7. Conclusion

Vertebrates' morphology and kinematic dimensional complexity make the design of biomimetic robots with equivalent complexity infeasible. Given the stringent weight limits

and power requirements in smaller animals, it is currently impossible to replicate their dimensional complexity in the context of biology-inspired robotics. Thus, topological simplifications must be made to reduce this complexity while still retaining the morphological properties of the biological system.

In this work, we propose a generic solution to replicate the prohibitively hard-to-mimic kinematic specializations found in biological systems with functionally versatile dynamic skeletal conformations based on characterizing key dominant modes and matching these modes in the space of principal components.

We applied a PCA-centered design paradigm to improve the performance of our bat-inspired robotic platform B2 by consolidating the mechanism of B2 with key biological modes such as wing folding–unfolding known to enhance the energetic efficiency of bat flight.

The bulky, compliant terminal organs in bat interact with their fluid environments and evidence suggests that folding the wings during the upstroke motion contributes to the efficiency of flight by curtailing the magnitude of the negative lift force, which acts antagonistically on the wings muscles. Following this design framework, such an energetic efficiency enhancement is achieved automatically as the kinematic synergies, which are the design descriptors and matched to those from bats, have direct influence on the aerodynamic terms.

First, a kinematic model of B2 was developed before presenting the synergistic design method to further the development of the geometric structure of B2 and shape its actuator trajectories over a wingbeat cycle. Further modifications were implemented by applying optimization of these synergies to find the behavior of B2 over a wingbeat and the physical parameters defining the constrained topology.

Second, B2 undertook a major hardware redesign based on coupling the flapping and folding–unfolding movements to accommodate the optimal solutions. The primary version of B2 was constructed with only five DoAs such that it exhibits synergies evident in biological bats. From a practical standpoint, this design cannot fit into the synergistic design that projects the rapid mediolateral movement of the forelimbs because the electric motors hosted in the original design of B2 have limited output power.

The numerical and experimental results obtained in this work validate the effectiveness of the synergistic design approach outlined in this article and confirm similar behavior of B2 to the biological bat through optimization of synergies. A major achievement is realized through reducing the high dimensional kinematics of bats. Although B2 has a significantly reduced dimensional complexity, it exhibits geometric movement like that of a biological bat (e.g., joint angles and marker positions). The optimization formulation depended on matching dominant principal components, and the results of matching joint angle progressions and marker trajectories between B2 and biology demonstrate the effectiveness of these synergies for selection of

geometric parameters and actuator inputs. In addition, the optimized folding–unfolding design showcases significant aerodynamic superiority over the fixed-wing case.

Folding and unfolding the wings within a wingbeat cycle is not only a significant achievement in itself, but it also creates new avenues of research for this project. A recent study considered the costs of hovering for insects, hummingbirds, and bats, and it concluded that the folding and unfolding phenomenon of bat flight allows some species to hover (Vejdani et al., 2017). Thus, B2's capability to fold its wings during the upstroke may allow hovering to be possible, as well as other advanced and challenging flight maneuvers. This greatly extends the capabilities of this robotic platform.

Performance and efficiency can further be improved through addressing limitations of the newly designed folding system. This flapping and folding mechanisms are systems of rigid linkages that both connect to the crank arm, and consequently there is latency in the transitions of wing folding and flapping. The large wing inertia exerts varying torques to the crank, and energy is lost at points of high torque that the BLDC must overcome. Biological bats avoid these difficulties by harnessing elasticity of their tendons to recover energy over the course of the wingbeat period (Konow et al., 2015). Similarly, we can reduce energy loss in B2 by the addition of compliant elements that can store energy during periods of high torque and release the energy later in the period. In future works, we will consider replacing some elements of the coupling mechanism with compliant linkages to reduce torque load on the motor and store elastic energy.

Folding during the upstroke improved lift performance with minor thrust penalties, but the redesign of B2 eliminated the two control actions of asynchronous mediolateral wing morphing that aid in roll stabilization. However, this actuation can be reintroduced to recover these lost DoAs by active manipulation of the configuration of the coupling mechanism. For example, motors can reposition the rocker arms of the coupling mechanism on either side to change the folding amplitudes of the wings in real time. Asynchronous control of folding amplitude will produce similar effects as direct actuation of the spindles because this allows average wing area on either side to be controlled, thus changing the aerodynamic torque on the system.

It is worth noting that the resulting kinematics is not guaranteed to yield stable flight dynamics. This optimization design procedure is based solely on kinematic behavior; aerodynamic forces are not considered. Closed-loop feedback is necessary and is addressed in separate works.

Acknowledgments

We would like to thank the team of graduate and undergraduate students from aerospace, electrical, computer, and mechanical engineering departments at the University of Illinois at Urbana-Champaign for their contribution to construct the initial prototype

of B2. The biological motion capture data set was provided by Kenneth Breuer and Sharon Swartz from Brown University. We greatly appreciate their insights and helpfulness in this project. We would like to thank them in their assistance with this, as well as José Iriarte-Díaz for compiling the data. The experimental results were performed in the Intelligent Robotics Laboratory (IRL) of the Coordinated Science Laboratory Studio.

Funding

This research was supported by the NSF (grant number 1427111).

Notes

1. Dorsal is the direction towards the back of the bat, and ventral is pointed towards the stomach. This is elevation–depression (up–down) movement.
2. Wrist pronation is the movement of the wrist angle with respect to body pitch.
3. Flexion means a bending motion that decreases the angle between two attached segments, and extension is a stretching motion that increases this angle.
4. Abduction refers to the motion of an appendage away from the midline of the body or another appendage, and adduction refers to moving or pulling towards the midline.
5. Medial is towards the body centerline, lateral is away from it. This is side to side motion.
6. Plane offset from the plane dividing the body into right and left halves.

References

- Ananthanarayanan A, Azadi M and Kim S (2012) Towards a bio-inspired leg design for high-speed running. *Bioinspiration and Biomimetics* 7(4): 046005.
- Artemiadis PK and Kyriakopoulos KJ (2010) EMG-based control of a robot arm using low-dimensional embeddings. *IEEE Transactions on Robotics* 26(2): 393–398.
- Bahlman JW, Swartz SM and Breuer KS (2013) Design and characterization of a multi-articulated robotic bat wing. *Bioinspiration & Biomimetics* 8(1): 016009.
- Bernstein NA (1967) *The coordination and regulation of movements*. Oxford: Pergamon Press.
- Bicchi A, Gabbicini M and Santello M (2011) Modelling natural and artificial hands with synergies. *Philosophical Transactions of the Royal Society B: Biological Sciences* 366(1581): 3153–3161.
- Birch MC, Quinn RD, Hahn G, et al. (2000) Design of a cricket microrobot. *IEEE International Conference on Robotics and Automation (ICRA)* 2: 1109–1114.
- Brown CY and Asada HH (2007) Inter-finger coordination and postural synergies in robot hands via mechanical implementation of principal components analysis. *IEEE/RSJ International Conference on Intelligent Robots and Systems (IROS)*, pp. 2877–2882.
- Butterfaß J, Grebenstein M, Liu H and Hirzinger G (2001) DLR-Hand II: Next generation of a dextrous robot hands. *IEEE International Conference on Robotics and Automation (ICRA)*, vol. 1, pp. 109–114.
- Cappellini G, Ivanenko YP, Poppele RE and Lacquaniti F (2006) Motor patterns in human walking and running. *Journal of Neurophysiology* 95(6): 3426–3437.
- Catalano MG, Grioli G, Farnioli E, Serio A, Piazza C and Bicchi A (2014) Adaptive synergies for the design and control of the Pisa/IIT SoftHand. *The International Journal of Robotics Research* 33(5): 768–782.
- Catalano MG, Grioli G, Serio A, Farnioli E, Piazza C and Bicchi A (2012) Adaptive synergies for a humanoid robot hand. In: *IEEE-RAS International Conference on Humanoid Robots*, pp. 7–14.
- Cheney JA, Ton D, Konow N, Riskin DK, Breuer KS and Swartz SM (2014) Hindlimb motion during steady flight of the lesser dog-faced fruit bat, *Cynopterus brachyotis*. *PLoS ONE* 9(5): e98093.
- Chung SJ and Dorothy M (2010) Neurobiologically inspired control of engineered flapping flight. *Journal of Guidance, Control, and Dynamics* 33(2): 440–453.
- Ciocarlie M, Goldfeder C and Allen P (2007) Dimensionality reduction for hand-independent dexterous robotic grasping. In: *IEEE/RSJ International Conference on Intelligent Robots and Systems (IROS)*, pp. 3270–3275.
- Ciocarlie MT and Allen PK (2009) Hand posture subspaces for dexterous robotic grasping. *The International Journal of Robotics Research* 28(7): 851–867.
- Colorado J, Barrientos A, Rossi C, Bahlman JW and Breuer KS (2012) Biomechanics of smart wings in a bat robot: morphing wings using SMA actuators. *Bioinspiration and Biomimetics* 7(3): 036006.
- Daffertshofer A, Lamoth CJC, Meijer OG and Beek PJ (2004) PCA in studying coordination and variability: a tutorial. *Clinical Biomechanics* 19(4): 415–428.
- d’Avella A, Saltiel P and Bizzi E (2003) Combinations of muscle synergies in the construction of a natural motor behavior. *Nature Neuroscience* 6(3): 300–308.
- Deng X, Schenato L and Sastry SS (2006a) Flapping flight for biomimetic robotic insects: Part II-flight control design. *IEEE Transactions on Robotics* 22(4): 789–803.
- Deng X, Schenato L, Wu WC and Sastry SS (2006b) Flapping flight for biomimetic robotic insects: Part I-system modeling. *IEEE Transactions on Robotics* 22(4): 776–788.
- Fod A, Mataric MJ and Jenkins OC (2002) Automated derivation of primitives for movement classification. *Autonomous Robots* 12(1): 39–54.
- Gabbicini M, Bicchi A, Prattichizzo D and Malvezzi M (2011) On the role of hand synergies in the optimal choice of grasping forces. *Autonomous Robots* 31(2–3): 235–252.
- Gong C, Travers MJ, Astley HC, et al. (2016) Kinematic gait synthesis for snake robots. *The International Journal of Robotics Research* 35(1–3): 100–113.
- Hoff J, Ramezani A, Chung SJ and Hutchinson S (2016) Synergistic design of a bio-inspired micro aerial vehicle with articulated wings. In: *Robotics: Science and Systems (RSS)*.
- Hoff J, Ramezani A, Chung SJ and Hutchinson S (2017) Reducing versatile bat wing conformations to a 1-dof machine. *Living Machines 2017: Biomimetic and Biohybrid Systems*. New York: Springer, pp. 181–192.
- Hubel TY, Hristov NI, Swartz SM and Breuer KS (2012) Changes in kinematics and aerodynamics over a range of speeds in *Tadarida brasiliensis*, the Brazilian free-tailed bat. *Journal of The Royal Society Interface* 9(71): 1120–1130.

- Jolliffe I (2002) *Principal Component Analysis*. New York: John Wiley & Sons, Ltd.
- Keennon M, Klingebiel K and Won H (2012) Development of the nano hummingbird: A tailless flapping wing micro air vehicle. *50th AIAA Aerospace Science Meeting*.
- Konow N, Cheney JA, Roberts TJ, Waldman JRS and Swartz SM (2015) Spring or string: does tendon elastic action influence wing muscle mechanics in bat flight? *Proceedings of the Royal Society of London B: Biological Sciences* 282(1816): 20151832.
- Laksanacharoen S, Pollack AJ, Nelson GM, Quinn RD and Ritzmann RE (2000) Biomechanics and simulation of cricket for microrobot design. In: *IEEE International Conference on Robotics and Automation (ICRA)*, vol. 2, pp. 1088–1094.
- Lim B, Ra S and Park FC (2005) Movement primitives, principal component analysis, and the efficient generation of natural motions. In: *IEEE International Conference on Robotics and Automation (ICRA)*, pp. 4630–4635.
- Lin J, Wu Y and Huang TS (2000) Modeling the constraints of human hand motion. In: *IEEE Workshop on Human Motion*, pp. 121–126.
- Liu GH, Lin HY, Lin HY, Chen ST and Lin PC (2014) A bio-inspired hopping kangaroo robot with an active tail. *Journal of Bionic Engineering* 11(4): 541–555.
- Ma KY, Chirarattananon P, Fuller SB and Wood RJ (2013) Controlled flight of a biologically inspired, insect-scale robot. *Science* 340(6132): 603–607.
- Mason CR, Gomez JE and Ebner TJ (2001) Hand synergies during reach-to-grasp. *Journal of Neurophysiology* 86(6): 2896–2910.
- Norberg UM (1972) Functional osteology and myology of the wing of the dog-faced bat *Rousettus aegyptiacus* (E. Geoffroy)(Mammalia, Chiroptera). *Zeitschrift für Morphologie der Tiere* 73(1): 1–44.
- Norberg UM and Rayner JM (1987) Ecological morphology and flight in bats (Mammalia; Chiroptera): wing adaptations, flight performance, foraging strategy and echolocation. *Philosophical Transactions of the Royal Society B: Biological Sciences* 316(1179): 335–427.
- Paranjape AA, Chung SJ and Kim J (2013) Novel dihedral-based control of flapping-wing aircraft with application to perching. *IEEE Transactions on Robotics* 29(5): 1071–1084.
- Pines DJ and Bohorquez F (2006) Challenges facing future micro-air-vehicle development. *AIAA Journal of Aircraft* 43(2): 290–305.
- Platzer MF, Jones KD, Young J and Lai JCS (2008) Flapping wing aerodynamics: progress and challenges. *AIAA Journal* 46(9): 2136–2149.
- Ramezani A, Chung SJ and Hutchinson S (2017) A biomimetic robotic platform to study flight specializations of bats. *Science Robotics* 2(3): eaal2505.
- Ramezani A, Shi X, Chung SJ and Hutchinson S (2015) Lagrangian modeling and flight control of articulated-winged bat robot. In: *IEEE/RSJ International Conference on Intelligent Robots and Systems (IROS)*, pp. 2867–2874.
- Ramezani A, Shi X, Chung SJ and Hutchinson S (2016a) Bat Bot (B2), a biologically inspired flying machine. In: *IEEE International Conference on Robotics and Automation (ICRA)*, pp. 3219–3226.
- Ramezani A, Shi X, Chung SJ and Hutchinson S (2016b) Modeling and nonlinear flight controller synthesis of a bat-inspired micro aerial vehicle. In: *AIAA Guidance, Navigation, and Control Conference*, p. 1376.
- Riskin DK, Bergou A, Breuer KS and Swartz SM (2012) Upstroke wing flexion and the inertial cost of bat flight. *Proceedings of the Royal Society of London B: Biological Sciences* 279(1740): 2945–2950.
- Riskin DK, Willis DJ, Iriarte-Daiz J, et al. (2008) Quantifying the complexity of bat wing kinematics. *Journal of Theoretical Biology* 254(3): 604–615.
- Santello M, Flanders M and Soechting JF (1998) Postural hand synergies for tool use. *The Journal of Neuroscience* 18(23): 10105–10115.
- Shyy W, Aono H, Chimakurthi SK, et al. (2010) Recent progress in flapping wing aerodynamics and aeroelasticity. *Progress in Aerospace Sciences* 46(7): 284–327.
- Taix M, Tran MT, Souères P and Guigon E (2013) Generating human-like reaching movements with a humanoid robot: A computational approach. *Journal of Computational Science* 4(4): 269–284.
- Tangorra JL, Davidson SN, Hunter IW, et al. (2007) The development of a biologically inspired propulsor for unmanned underwater vehicles. *IEEE Journal of Oceanic Engineering* 32(3): 533–550.
- Tian X, Iriarte-Diaz J, Middleton K, et al. (2006) Direct measurements of the kinematics and dynamics of bat flight. *Bioinspiration and Biomimetics* 1(4): S10–S18.
- Torres-Oviedo G and Ting LH (2007) Muscle synergies characterizing human postural responses. *Journal of Neurophysiology* 98(4): 2144–2156.
- Vejdani H, Boerma D, Swartz SM and Breuer KS (2017) Guidelines for the design and control of bio-inspired hovering robots. In: *IEEE International Conference on Robotics and Automation (ICRA)*, pp. 4160–4166.
- Wang L, Tan T, Ning H and Hu W (2003) Silhouette analysis-based gait recognition for human identification. *IEEE Transactions on Pattern Analysis and Machine Intelligence* 25(12): 1505–1518.
- Wang M, Zang X, Fan J and Zhao J (2008) Biological jumping mechanism analysis and modeling for frog robot. *Journal of Bionic Engineering* 5(3): 181–188.

Appendix. Index to multimedia extensions

Archives of IJRR multimedia extensions published prior to 2014 can be found at <http://www.ijrr.org>, after 2014 all videos are available on the IJRR YouTube channel at <http://www.youtube.com/user/ijrrmultimedia>

Table of Multimedia Extensions

Extension	Media type	Description
1	Video	High-speed footage of designed mechanism showing the coupled motion between flapping and folding-unfolding over a wingbeat period.